Acta Oceanol. Sin., 2022, Vol. 41, No. 10, P. 74–93
https://doi.org/10.1007/s13131-022-2006-4
http://www.aosocean.com
E-mail: ocean2@hyxb.org.cn

Three-dimensional characteristics of mesoscale eddies simulated by a regional model in the northwestern Pacific Ocean during 2000–2008

Guijing Yang[1], Xiayan Lin[1, 2*], Guoqing Han[1], Yu Liu[1, 3], Gengxin Chen[4], Jianhui Wang[1]

[1] Marine Science and Technology College, Zhejiang Ocean University, Zhoushan 316000, China

[2] State Key Laboratory of Satellite Ocean Environment Dynamics, Second Institute of Oceanography, Ministry of Natural Resources, Hangzhou 310012, China

[3] Southern Marine Science and Engineering Guangdong Laboratory (Zhuhai), Zhuhai 519082, China

[4] State Key Laboratory of Tropical Oceanography, South China Sea Institute of Oceanology, Chinese Academy of Sciences, Guangzhou 510301, China

Received 24 September 2021; accepted 11 February 2022

Abstract

Mesoscale eddies play vital roles in ocean processes. Although previous studies focused on eddy surface features and individual three-dimensional (3D) eddy cases in the northwestern Pacific Ocean, the analysis of unique eddy 3D regional characteristics is still lacking. A 3D eddy detection scheme is applied to 9 years (2000–2008) of eddy-resolving Regional Ocean Modeling System (ROMS) output to obtain a 3D eddy dataset from the surface to a depth of 1 000 m in the northwestern Pacific Ocean (15°–35°N, 120°–145°E). The 3D characteristics of mesoscale eddies are analyzed in two regions, namely, Box1 (Subtropical Countercurrent, 15°–25°N, 120°–145°E) and Box2 (Southern Kuroshio Extension, 25°–35°N, 120°–145°E). In Box1, the current is characterized by strong vertical shear and weak horizontal shear. In Box2, the current is characterized by the strong Kuroshio, topographic effect, and the westward propagation of Rossby waves. The results indicate the importance of baroclinic instability in Box1, whereas in Box2, both the barotropic and baroclinic instability are important. Moreover, the mesoscale eddies' properties in Box1 and Box2 are distinct. The eddies in Box1 have larger number and radius but a shorter lifetime. By contrast, Box2 has fewer eddies, which have smaller radius but longer lifetime. Vertically, more eddies are detected at the subsurface than at the surface in both regions; the depth of 650 m is the turning point in Box1. Above this depth, the number of cyclonic eddies (CEs) is larger than that of anticyclonic eddies (AEs). In Box2, the number of CEs is dominant vertically. Eddy kinetic energy (EKE) and mean normalized relative vorticity in Box2 are significantly higher than those in Box1. With increasing depth, the attenuation trend of EKE and relative vorticity of Box1 become greater than those of Box2. Furthermore, the upper ocean (about 300 m in depth) contains 68.6% of the eddies (instantaneous eddy). Only 16.6% of the eddies extend to 1 000 m. In addition, about 87% of the eddies are bowl-shaped eddies in the two regions. Only about 3% are cone-shaped eddies. With increasing depth of the eddies, the proportion of bowl-shaped eddies gradually decreases. Conversely, the cone- and lens-shaped eddies are equal in number at 700–1 000 m, accounting for about 30% each. Studying the 3D characteristics of eddies in two different regions of the northwestern Pacific Ocean is an important stepping stone for discussing the different eddy generation mechanisms.

Key words: three-dimensional structures, mesoscale eddies, northwestern Pacific Ocean

Citation: Yang Guijing, Lin Xiayan, Han Guoqing, Liu Yu, Chen Gengxin, Wang Jianhui. 2022. Three-dimensional characteristics of mesoscale eddies simulated by a regional model in the northwestern Pacific Ocean during 2000–2008. Acta Oceanologica Sinica, 41(10): 74–93, doi: 10.1007/s13131-022-2006-4

1 Introduction

Mesoscale eddies are distributed ubiquitously in the world's oceans. They contain a considerable amount of kinetic energy, which can account for ~90% of the total energy of ocean circulation (Su et al., 2001; Wunsch and Ferrari, 2004; Jing et al., 2021). They play critical roles in ocean dynamics, heat, salinity and energy transport, and biogeochemical processes (McNeil et al., 1999; McGillicuddy et al., 1999; Stammer, 1998; Chelton et al., 2011a, b; Dong et al., 2017; Sun et al., 2019), as well as in air-sea interactions (Lin et al., 2019; Ma et al., 2015). Mesoscale eddy

Foundation item: The National Natural Science Foundation of China under contract Nos NSFC 41806030 and 42076021; the China Ocean Mineral Resources Research and Development Association Program under contract No. DY135-E2-3-01; the Basic Scientific Research Business Expenses of Zhejiang Provincial Universities under contract No. 2020J00007; the project of State Key Laboratory of Tropical Oceanography, South China Sea Institute of Oceanology, Chinese Academy of Sciences under contract No. LTO1807; the project of Southern Marine Science and Engineering Guangdong Laboratory (Zhuhai) under contract No. SML2020SP007; the Innovation Group Project of Southern Marine Science and Engineering Guangdong Laboratory (Zhuhai) under contract No. 311020004; the Strategic Priority Research Program of Chinese Academy of Sciences under contract No. XDB42000000.
*Corresponding author, E-mail: linxiayan@zjou.edu.cn

activity strongly affects wind variations (Lin et al., 2019), thus impacting climate-relevant ocean mean and variability simulations (Chassignet et al., 2020). The divergent effects of cyclonic eddies (CEs) and convergent effects of anticyclonic eddies (AEs) have distinct impacts on ocean vertical mixing. The construction of a unified three-dimensional (3D) eddy structure helps elucidate the transport capability of eddies (Zhang et al., 2013, 2014; Dong et al., 2014; Wang et al., 2020a). Additionally, accurate prediction of oceanic mesoscale eddies propagation and magnitudes helps elucidate synoptic to intra-seasonal time scales ocean forecast and prediction (Meng et al., 2021).

The northwestern Pacific Ocean (NWPO; 15°–35°N, 120°–145°E) has a very complex ocean circulation system (Fig. 1) because of its geographical position adjacent to the western boundary of the Pacific Ocean (Qu et al., 1998). The westward Northern Equatorial Current (NEC) reaches the coast of the Philippines and bifurcates near 13°N due to the influence of topography (Toole et al., 1990; Wang et al., 2009; Zhou et al., 2006), thereby forming the equatorial Mindanao Current (MC) and the poleward Kuroshio Current (KC). In addition, the Kuroshio, which carries warm, salty equatorial water, gradually strengthens while flowing along the western boundary. This extremely energetic western boundary current eventually forms the Kuroshio extension region along the coast of Japan at 35°N (Chern et al., 1990; Qiu and Imasato, 1990). The Pacific western boundary currents (WBCs, NEC-MC-KC, and NMK currents system) in the NWPO also play a very important role in the global ocean circulation and local climate systems. The WBCs' flow strength and weakness have important effects on heat, salt, and energy exchange between the equatorial Pacific and the subtropical Pacific. With global warming, the change of the Western Pacific Boundary current directly affects the Indonesian Throughflow (ITF), which in turn affects the global thermohaline circulation (GTHC) and global climate change (Gordon, 1986; Hu et al., 2015; Lukas et al., 1991, 1996; McCreary and Lu, 1994; Zhou et al., 2006). Meanwhile, high mesoscale eddy activities exist in the NWPO, especially in the Subtropical Countercurrent (STCC) region, as well as in the Kuroshio region and its extension. The baroclinic instability from the vertical shear between STCC and NEC is the main energy source for eddies in the STCC region (Qiu, 1999; Roemmich and Gilson, 2001; Qiu and Chen, 2005, 2010; Noh et al., 2007; Kang et al., 2010; Liu et al., 2012; Zhou et al., 2021). In the Kuroshio and its extension area, the horizontal shear and vertical buoyancy flux on the two sides of the Kuroshio axis are important energy sources for eddies (Liu et al., 2017a). With decreasing significance of the topography, the instability of strong currents can lead to large and small bends. When the loops formed by the bends pinch off, the eddies break away from the main axis (Chern et al., 1990; Dai et al., 2020; Dong et al., 2017; Ji et al., 2018; Ma et al., 2016). A recent study showed that mesoscale eddies have a significant effect on the intra-seasonal variation of NEC bifurcation. These results provide valuable evidence for studying the role of mesoscale eddies in the NWPO (Zhou et al., 2010, 2021). Therefore, investigating the distribution and propagation characteristics of mesoscale eddies is important to elucidate the energy variation and air-sea interaction in this region.

In recent decades, many physical oceanographers have paid particular attention to mesoscale eddy activities in the NWPO, but most of them focused on eddy surface characteristics. For example, Lin (2005) used satellite altimetry data from 1993 to 2001 and found that an average of 60 mesoscale eddies were gener-

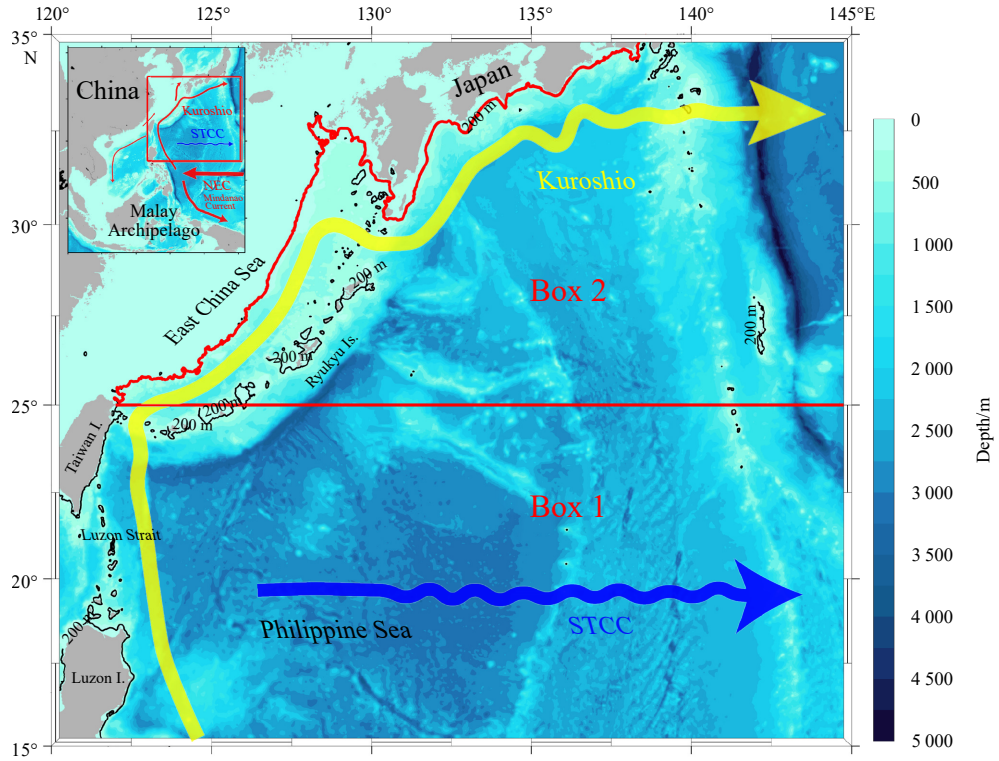

Fig. 1. Bathymetry of the study area (15°–35°N, 120°–145°E). 25°N (horizontal red line) and 200 m isobath (curved red line) are the dividing lines. South of 25°N defines Box1 (STCC , 15°–25°N, 120°–145°E), whereas north of 25°N and a water depth exceeding 200 m define Box2 (Southern Kuroshio Extension, SKE, 25°–35°N, 120°–145°E). The background color represents the water depth in unit of meter. The inset shows the model simulation domain. The topography data is from ETOPO1 (Amante and Eakins, 2009).

ated in the NWPO annually. The number of cold eddies was reportedly slightly higher than that of warm eddies. Furthermore, the mesoscale eddies also had noticeable seasonal variations, more eddies appeared in spring, and less appeared in autumn. More CEs than AEs with a lifetime longer than 30 d were observed (Cui et al., 2017). In the NWPO, the energy source of eddies might be baroclinic instability, and a reverse cascade of energy was found (Wang et al., 2019). Yang et al. (2019a) used a numerical model in the NWPO and found that the air-sea heat flux and wind stress in the Kuroshio Extension (KE) promote the dissipation of oceanic eddies. Moreover, the eddy-induced heat flux anomalies dampen the sea surface temperature (SST) anomalies, thereby dampening the available potential energy of eddies. This phenomenon significantly influences the large-scale SST in the Kuroshio-Oyashio extension region (Shan et al., 2020).

Satellite data can only reveal the surface characteristics of eddies, and *in-situ* data are scarce, thereby resulting in limited studies on the vertical structures of eddies in NWPO (Lin et al., 2012; Zheng et al., 2014; Cui et al., 2017). Argo data is commonly used to analyze individual cases of 3D eddies, study the vertical thermohaline structure of eddies, and synthesize 3D eddy structure (Chaigneau et al., 2011; Yang et al., 2019b; de Marez et al., 2019; Aguedjou et al., 2019). He (2007) found that AEs were mostly bowl-shaped, and their depth could reach 1 000–2 000 m in NWPO. The CEs were more cylindrical and shallower; they usually reach only a few hundred meters. Zhang et al. (2015) used Argo floats and reported two sub-thermocline anticyclonic lens-shaped eddies in the subtropical NWPO, with depths lower than 600 m and thickness values between 150 m and 190 m. Wang et al. (2020a) observed an AE between 400 m and 600 m in the same area. The maximum temperature and salinity anomalies of the eddy core were 1.7°C (1.9°C) and 0.04 (0.07) in the growing stage (further growing stage), respectively. The temperature and salinity anomaly centers of the AE were between 500 m and 600 m and 800 m and 900 m, respectively (Dai et al., 2020). Liu et al. (2012) used more than 3 000 Argo float profiles and satellite altimeter data to statistically analyze the vertical thermohaline structure of mesoscale eddies in the subtropical countercurrent area. The cold- and warm-core depths of cold and warm eddies were similar, and the maximum temperature anomalies were around 1°C . Yang et al. (2013) explained that due to the existence of mode waters in the main thermocline, the eddy-induced temperature anomaly of CEs exhibited a double-core vertical structure. However, the salinity anomaly of AEs was significantly sandwich-shaped because of the vertical water mass distribution. In addition, in-depth understanding of eddies 3D structure only focused on the Kuroshio Extension (Yuan et al., 2021). A cylindrical eddy was based on three existing eddy shapes, and its radius was almost consistent across all layers. By using high spatial resolution Argo data, the 3D structure of single eddy or composite eddies can be obtained (Zhang et al., 2013, 2015; Sun et al., 2017; Wang et al., 2020a; Dai et al., 2020), but the detailed evolution processes of eddies are difficult to trace. Therefore, the statistical results of 3D eddy structures can be obtained only by high resolution model output.

Previous mesoscale eddy studies in the NWPO focused on the statistics of surface features, few individual 3D eddy cases, eddies' vertical temperature and salinity structures, heat/salt transport, and eddy-induced air-sea interactions. The lack of 3D eddy features limits the understanding of eddy behavior, including the generation, maintenance, and decay of 3D eddies, as well as the different generation and termination mechanisms in different parts of the NWPO. The 3D characteristics of mesoscale eddy in the NWPO are analyzed in this paper by applying a 3D eddy detection method to 9 years (2000–2008) of the Regional Ocean Modeling System (ROMS) model data.

The rest of the paper is organized as follows. Section 2 introduces the data and methods used to detect 3D eddies. Sections 3–5 analyze the 3D characteristics and structures of eddies, the distribution of three types of eddies in different regions, and the 3D horizontal and vertical profiles of temperature, salinity, and velocity, respectively. Section 6 shows the conclusions.

2 Data and methods

2.1 *Observation data*

The archiving, validation and interpretation of satellite oceanographic (AVISO, http://www.aviso.altimetry.fr/) sea surface height anomaly and geostrophic flow anomaly data provided by Copernicus Marine Environment Monitoring Service Center (CMEMS, http://www.copernicus.eu/) are used. The daily data have a spatial resolution of (1/4)°×(1/4)° and are obtained from January 1993 to December 2019. The Chelton's eddy dataset (eddy_trajectory_2.0exp_19 930 101_20 191 015) is also provided by AVISO. The dataset includes eddy trajectory, center, radius, amplitude, rotation velocity, and polarity based on the results of daily sea level anomaly detection from January 1993 to October 2019.

The SST data are from the operational sea surface temperature and ice analysis (OSTIA) data provided by CMEMS (https://resources.marine.copernicus.eu/, SST_GLO_SST_L4_REP_OBSERVATIONS_010_011). This dataset is a combination of satellite and *in situ* data and extends from October 1981 to the present. It has a temporal resolution of 1 d and a spatial resolution of (1/20)°×(1/20)°.

To have a similar period as the ROMS model data, only data obtained from 2000 to 2008 are selected from the above datasets.

2.2 *Model output*

This study uses the results from ROMS. The sea surface thermal forcing fields, such as 2 m air temperature, skin temperature, rainfall rate, 2 m absolute humidity, upward/downward long-wave radiation fluxes, and upward/downward short-wave radiation fluxes, are derived from the National Centers for Environmental Prediction (NCEP)/ National Center for Atmospheric Research (NCAR) Reanalysis1 daily atmospheric dataset available from 1958 to 2008 (http://www.esrl.noaa.gov/psd/data/gridded/data.ncep.reanalysis.surfaceflux.html). The heat fluxes are calculated using the bulk formula. The 1958 simple ocean data assimilation (SODA) products, including ocean temperature, salinity, currents, and sea surface height at a resolution of (1/2)° and interpolated to (1/12)°, are used as the initial field. A warm start is adopted. Considering that the integration is initialized in January 1958, the surface forcing and cyclic boundary conditions from January to December of that year is adopted for 10 years. From 1958 to July 1999, the wind field data of NCEP/NCAR Reanalysis 1 are used as the atmospheric dynamic forcing field. Considering that the resolution of the NCEP/NCAR forcing is (1/2)°, we shift to a blended wind field with a (1/4)° resolution from August 1999 to 2008, in accordance with the QuikScat wind measurement data (https://manati.star.nesdis.noaa.gov/products/QuikSCAT.php). The western boundary is closed, and the three other boundaries are open in our model domain. We select the Chapman scheme for the barotropic open boundary (Chapman, 1985) and the radiation scheme for the baroclinic open boundary (Orlanski, 1976; Raymond and Kuo, 1984). A 10-year spin-up

was conducted for dynamic modification until stable variations are reached for the kinetic and eddy kinetic energy (EKE).

The model domain spans 9°S–41°N and 99°–145°45′E with a (1/12)° horizontal spatial resolution. In the vertical direction, a σ coordinate system with 32 equal layers is adopted. The K-Profile parameterization (KPP) mixing scheme is used. The NWPO (15°–35°N, 120°–145°E) is selected as the study area from 2000 to 2008. For further analyses, the dataset is linearly interpolated to 21 vertical layers, as follows: 10 m, then every 50 m from 50 m to 1 000 m. The detailed settings of the model are found in Lin et al. (2013, 2015). The model evaluation is presented in Appendix. The model data have been used to study the 3D eddies in the South China Sea and have been verified (Lin et al., 2013, 2015). The ROMS model used in the present study does not include data assimilation, and the numerical results are dynamically balanced.

2.3 *Eddy detection scheme*

2.3.1 *Vector geometry-based surface eddy detection algorithm*

This paper adopts an automated mesoscale eddy detection method based on the geometric characteristics of the flow field, as proposed by Nencioli et al. (2010). Compared with the Okubo-Weiss method (Okubo, 1970; Weiss, 1991) and Winding-Angle method (Sadarjoen and Post, 2000), the selected method can detect eddies more efficiently and flexibly in complex velocity fields and has a higher rate of successful identification and a lower rate of excessive identification (Nencioli et al., 2010). This method has been widely used to study eddies in different sea areas around the world (Dong et al., 2012; Liu et al., 2012; Lin et al., 2015; Ma et al., 2016; Sun et al., 2018; Ji et al., 2018; Yang et al., 2020). Please refer to the above studies for more details on the eddy detection algorithm.

2.3.2 *Three-dimensional eddy detection method*

The eddy detection method introduced in Section 2.3.1 is applied to the 21 layers of velocity field to obtain the eddy position, polarity, radius, energy, and generation and decay time. It is assumed that the center of an eddy in the next layer does not drift more than 0.25 times of its upper layer's radius (at intervals of 50 m or less). We start from the surface and move down with the same polarity and occurrence time. If the eddy is found in the next layer, then we use the eddy information at that layer to continue searching in the layer below up to the 1 000 m layer. If no eddy is detected in the next layer, then we consider the depth of the eddy in the previous layer as the next layer's depth. Specific details about this method are found in Dong et al. (2012) and Lin et al. (2015).

3 Verification of eddy dataset and basis for regional division

3.1 *Validation of eddy dataset*

After applying the automated eddy detection method to the flow field of the 2000–2008 model data, the occurrence frequency of eddies with different lifetimes and radiuses are counted. Most eddies have a lifetime of 3–4 weeks, and a radius of 25–30 km (Appendix Fig. A4). Notably, due to the limitation of model resolution ((1/12)°×(1/12)°), the current method can only correctly identify eddies larger than 20 km. Therefore, this paper defines mesoscale eddies as eddies with a lifetime longer than 3 weeks and a radius larger than 30 km. In the subsequent analyses, we remove the eddies that do not meet these requirements. After screening, a total of 1 876 eddies remains (963 CEs and 913 AEs). On average, 208 eddies are generated annually, and this number is larger than the number reported by Lin et al. (2012) (150–151). The difference may be due to the addition of the East China Sea in our study and the differences in the studies' definition of mesoscale eddy lifetime. Lin et al. (2012) used a lifetime of 4 weeks.

We count the eddies by treating the entire eddy lifetime as one eddy and selecting the daily radius as the unit for counting radius. Figure 2 is obtained by filtering the eddy detection results from ROMS, AVISO, and the Chelton's eddy dataset (Chelton et al., 2011b) according to the thresholds. From the perspective of

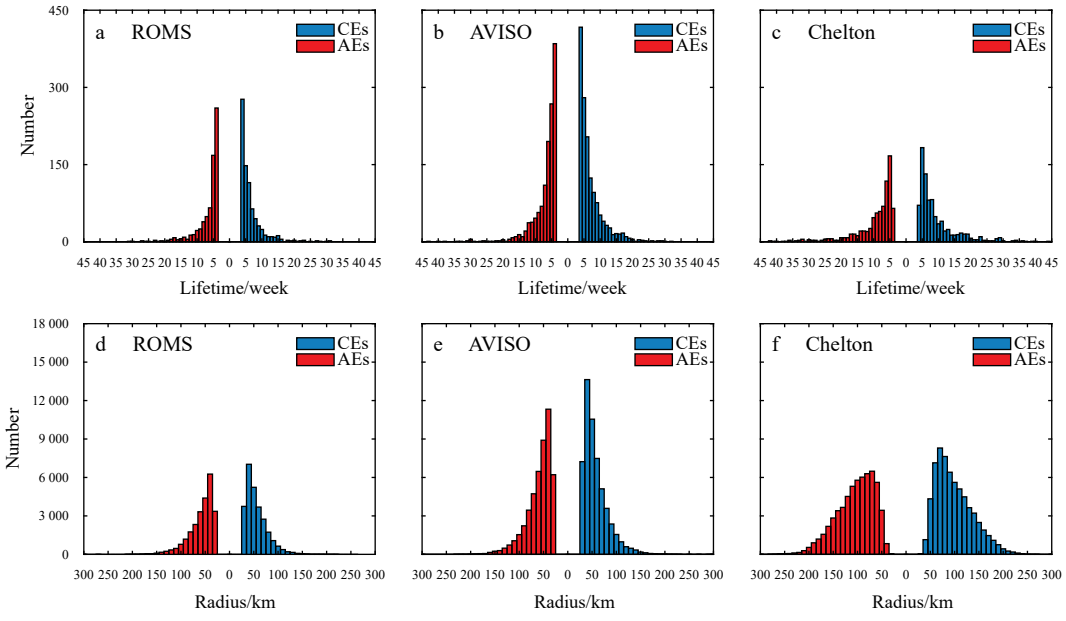

Fig. 2. Histograms of eddy lifetime (a, b, and c) and radius (d, e, and f) from ROMS output (left panels), AVISO data (middle panels), and Chelton's eddy dataset (right panels) from 2000 to 2008.

eddy lifetime and radius, they follow a normal distribution. The eddy lifetime is concentrated between 4 weeks and 6 weeks in the ROMS results. Only 14 CEs and 13 AEs have a lifetime longer than 21 weeks (Fig. 2a). The eddy lifetime from the AVISO results is also concentrated between 4 weeks and 6 weeks, but more short-lived eddies exist (Fig. 2b). The results from Chelton's eddy dataset also show a similar result, i.e., peaks at 4–6 weeks in the eddy lifetime (Fig. 2c), but more long-lived eddies exist. A total of 51 CEs and 57 AEs survived for more than 21 weeks. Compared with the lifetime, radius distributions of the CEs and AEs are also symmetrical (Figs 2d–f). The radius is within 150 km, and the peak radius appears at 30–50 km. Totally, 20 CEs and 98 AEs with a radius larger than 150 km are found (Fig. 2d), whereas 80 CEs and 101 AEs are noted in the AVISO data results (Fig. 2e). Among these large eddies, the mean radius of AEs is 20–30 km larger than that of CEs. The instantaneous eddy radius (Fig. 2f) is larger than that of the ROMS results, due to the fact that the eddies in Chelton's eddy dataset having a longer lifetime. The radius is mostly less than 250 km. More AEs than CEs exist for eddies with radius exceeding 250 km.

Based on the same eddy detection method, more eddies with a lifetime of 4–6 weeks and a radius of 30–50 km are detected in the AVISO data than in the ROMS model output. However, as shown by the original velocity field without setting any threshold (Appendix Fig. A3), the number of eddies detected from the model results is 12.8% more than that from AVISO data. The eddy number is smaller, but the eddies are larger in Chelton's eddy dataset. The main reason for this difference is the difference in the resolution of the two datasets. The original AVISO data have a spatial resolution of (1/4)°×(1/4)°, and the model output resolution is (1/12)°×(1/12)°. Although both datasets are interpolated to a (1/8)°×(1/8)° grid resolution, the model data can distinguish smaller eddies. Furthermore, the model output has a daily temporal resolution, whereas that of the original AVISO data is weekly. Several days of data are synthesized into 1 d; thus, similar information is retained. For this reason, eddies from the AVISO data have a longer lifetime. Although the mean lifetime and mean radius detected from the ROMS data are shorter and smaller than those from the AVISO and Chelton datasets, the number and lifetime distribution pattern of eddies obtained from the ROMS model are equivalent to those of Chelton's eddy dataset and AVISO data. Therefore, the eddy dataset obtained from the model is reliable and can be used to further study the 3D characteristics.

3.2 *Basis for regional division*

In previous studies on NWPO surface eddies, the region has always been regarded as a whole, but significant spatial differences in eddy polarity and intensity in the region are found in our study (Fig. 3). According to their differences, dividing NWPO into two areas is necessary for a comparative study. Figure 3a shows the eddy polarity distribution of the study area from 2000 to 2008, which reflects the dominant region of CEs and AEs. The definition of eddy polarity P refers to the probability that a certain point in the eddy is located in a CE ($P<0$) or an AE ($P>0$). The calculation method is expressed as Eq. (1), as follows:

$$P = \frac{F_{\mathrm{AE}} - F_{\mathrm{CE}}}{F_{\mathrm{AE}} + F_{\mathrm{CE}}}, \tag{1}$$

where F_{AE} and F_{CE} are the numbers of AEs and CEs appearing in each grid point (Chaigneau et al., 2009; Chen et al., 2011). Figure 3a shows that south of 20°N is dominated by CEs, and the AEs are widely distributed between 20°N and 25°N. This finding is consistent with that of Cheng et al. (2017), who revealed that eddies are very active between 14°N and 24°N, especially at two latitude bands, namely, 18°–19°N and 22°–23°N. In the western North Pacific, the eastward STCC is separated into three parts, namely, southern STCC (19°–20°N), northern STCC (22°–24°N), and eastern STCC (24°–27°N) (Hasunuma and Yoshida, 1978). In our study area (NWPO), the vertically meridional potential vorticity gradient of southern and northern STCC reverses and provides an energy source for the generation of eddies (Cheng et al., 2017). The number of AEs is significantly greater than that of CEs in the high-latitude regions of the Pacific Ocean (Zheng et al., 2014). A clear asymmetric distribution of eddy polarity exists in the Kuroshio area. CEs are generated on the left side of the Kuroshio, whereas AEs are generated on the right side. This finding is con-

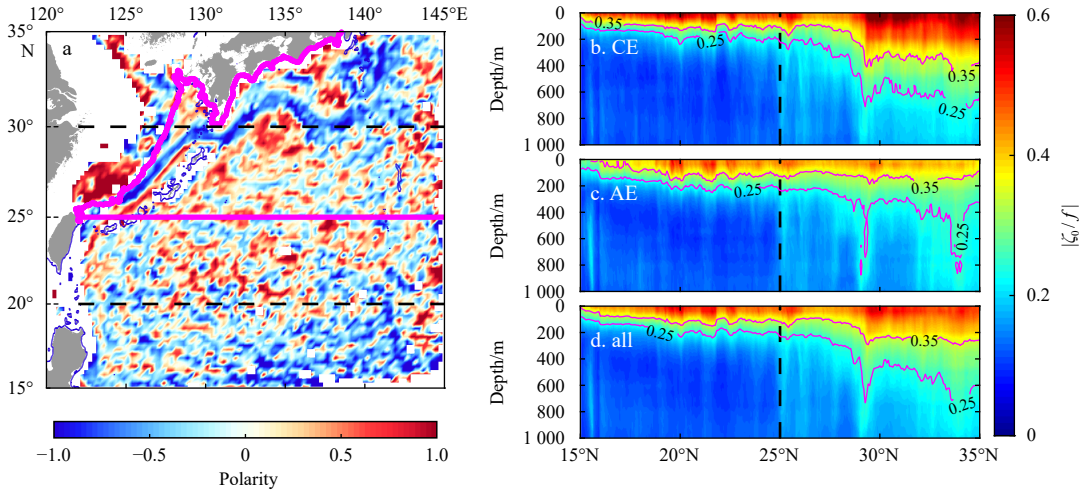

Fig. 3. Eddy polarity distribution map (a) and meridional vertical cross-section (zonal average of the whole domain) showing the average intensity of cyclonic (b), anticyclonic (c), and total eddies (d) during 2000–2008. In a, the blueish and reddish tones are cyclonic and anticyclonic eddies, respectively; the solid magenta line is the dividing line between Box1 and Box2. In b, the solid magenta lines are the contours of 0.25 and 0.35. The dotted lines in a are the dividing lines of every 5° of latitude, the dotted line in b marks latitude of 25°N.

sistent with the results of Liu et al. (2017a) along the main axis of the Kuroshio. The uniqueness of ocean eddies in western boundary current areas and the close relationship between the distribution of eddy polarity and the distribution of ocean current are highlighted (Chelton et al., 2011b).

To elucidate the influence of eddy depth, we divide the vorticity of the eddy center (ζ_0) by the Coriolis parameter (f) to obtain the relative vorticity (ζ_0/f) at the eddy center (Figs 3b and c). For both CEs or AEs, the larger eddies are concentrated in the upper ocean and show an axe shape with latitude. For CEs (Fig. 3b) with a relative vorticity greater than 0.25 at 200 m in the upper layer between 15°N and 25°N, the 0.25 contour line begins to deepen and reaches a depth of about 600 m as the latitude exceeds 25°N. However, the contour of AEs with intensity levels greater than 0.35 (Fig. 3c) remains above 200 m. From the 0.25 isoline, the depth begins to increase after 25°N, and two obvious protrusions are located at about 29°N and 34°N, where the depth can reach about 800 m. This phenomenon also appears in CEs, but the amplitude is relatively weak. After superposing the relative vorticity of CEs and AEs, the total trend of eddy intensity remains unchanged (Fig. 3d). With increasing latitude, the eddy intensity gradually deepens from 200 m. This phenomenon is related to the Kuroshio to the north of 25°N, which continuously provides energy to the eddies. In addition, previous studies have found that the number of eddies is small at south of 15°N (Yang et al., 2013), whereas the STCC (about 15°–25°N) and the southern Kuroshio Extension (SKE, about 25°–35°N) have high eddy activities (Wang et al., 2020). To understand the dynamic mechanisms linked to the distinct eddy characteristics of the two regions, we check the baroclinicity of the corresponding background ocean currents, according to Zhou et al. (2021). The horizontal shears (Fig. 4b) are calculated by averaging the absolute values of the meridional gradient of the zonal velocities between 15°N and 35°N. The vertical shears (Fig. 4c) are calculated by differencing the zonal velocities between vertical layers. The background flow fields in these two regions show distinct patterns. The current is characterized by strong vertical shear but weak horizontal shear at south of 25°N. This contributes to a high EKE level (Fig. 4a), indicating that baroclinic instability is the main energy source for eddies in this region. One of the dynamic mechanisms is the opposite directions of the surface STCC and subsurface NEC; other reasons are the opposite direction of the STCC and the westward propagation of Rossby waves and eddies in this region. The current is characterized by the strong Kuroshio, topography effect, and the westward propagation of Rossby waves north of 25°N. Two obvious regions with strong eddy relative vorticity (~29°N and ~34°N, Figs 3b–d) are observed. These areas also show very high EKE levels (Fig. 4a) due to the strong barotropic and baroclinic instability from surface to 1 000 m (Figs 4b and c). Therefore, considering the eddy polarity and intensity characteristics (Fig. 3), the study area is divided into Box1 (STCC, 15°–25°N, 120°–145°E) and Box2 (SKE, 25°–35°N, 120°–145°E). Eddies are then separately analyzed and counted in the two regions.

4 Eddy characteristics in Box1 and Box2

4.1 *Interannual, seasonal and monthly variations*

Box1 has 121 eddies a year on average, with small interannual variation (Fig. 5a). The largest number of eddies is 130 in 2000 and the smallest number is 111 in 2007. The numbers of CEs and AEs generated in different years also differ. In 2000, 68 AEs exist (maximum), whereas only 44 exist in 2007. In 2001 and 2008, up to 70 CEs exist, and in 2006, at least 56 exist. In 2007 and 2008, the numbers of CEs vastly exceed those of AEs by 23 and 18, respectively. A good correlation (0.54) exists between the interannual eddy number and EKE (not shown). The generation of mesoscale eddies has a clear seasonal variation (Fig. 5c). Spring has the maximum number of eddies; then, the number decreases

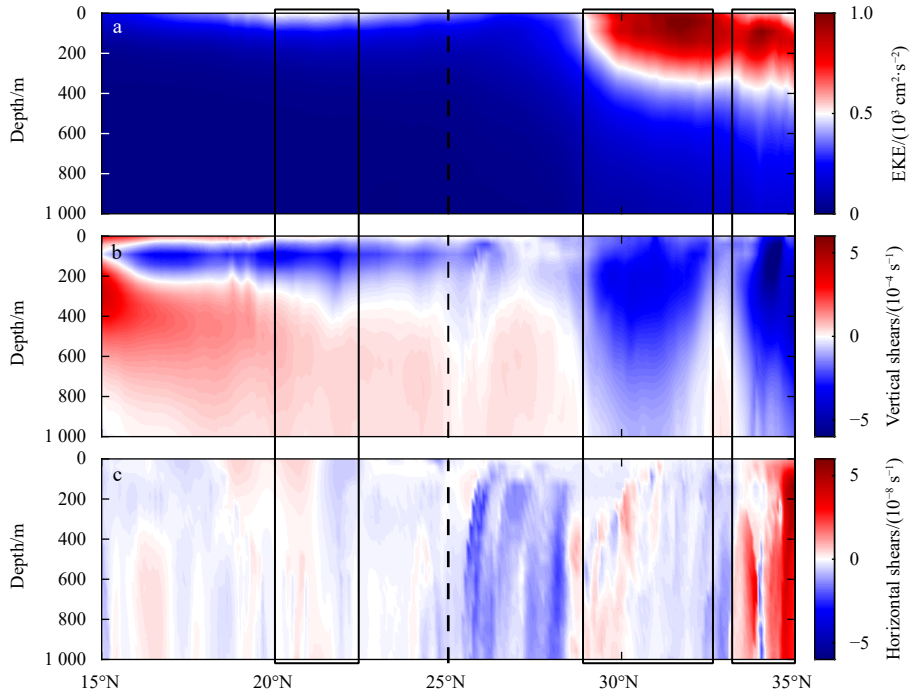

Fig. 4. Meridional cross-section (zonal average of the whole domain) of average EKE (a), vertical shear (b), and horizontal shear (c) during 2000–2008. The box is the corresponding position of Figs 3b–d corresponding to the high value area of EKE. The dotted line marks latitude of 25°N.

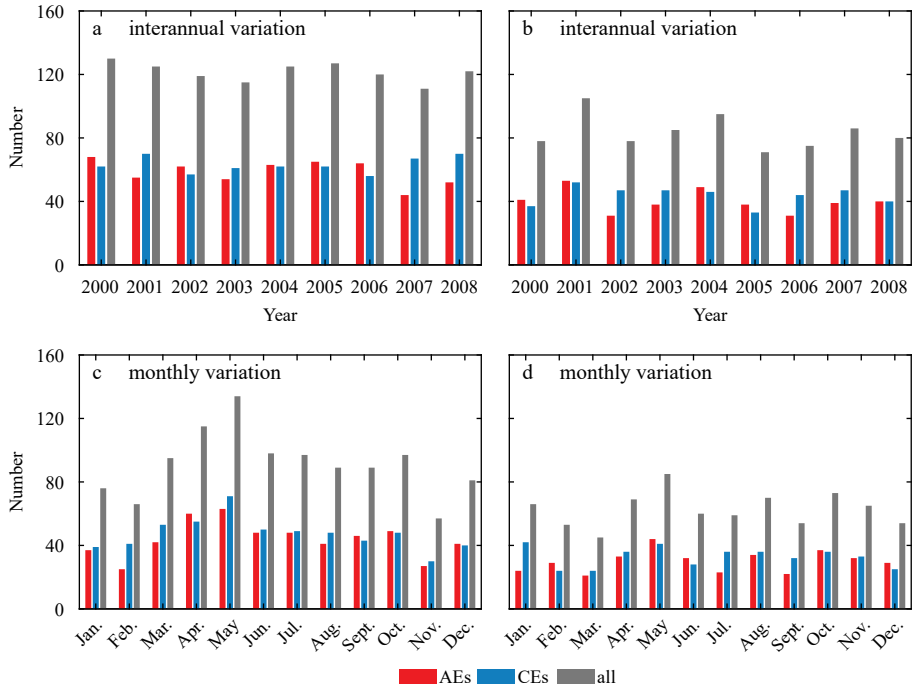

Fig. 5. Histograms of interannual (a and b) and monthly variation (c and d) in Box1 (left panels) and Box2 (right panels). Red, blue, and gray bars are the AEs, CEs, and total numbers, respectively.

with every subsequent season (spring: MAM, summer: JJA, autumn: SON, winter: DJF). The annual cycle of the number of eddies is more significant than the interannual variation (Fig. 5c). The number of generated eddies is highest in May and lowest in November, which corresponds to the summer and winter EKE seasonal variations, respectively (Qiu et al., 2014). This annual cycle of EKE is due to the seasonal changes in the STCC's intensity. The latter determines the growth rate of baroclinic instability (Qiu and Chen, 2013).

The number of eddies generated in Box2 is 83 per year on average and has a strong interannual variation (Fig. 5b). The highest and lowest numbers are 105 and 71 in 2001 and 2005, respectively. Similar to Box1, the number of CEs is different from that of AEs in the different years. The AEs and CEs reach maximum numbers of 53 and 52, respectively, in 2001. In the following year, the number of AEs decreases to a minimum of 31. That of CEs decreases to a minimum of 33 in 2005. The seasonal variation of the number of eddies generated in Box2 (Fig. 5d) is different from that in Box1. The numbers of CEs in spring and autumn are larger than those in summer and winter; there are more CEs than AEs. As for the monthly variation (Fig. 5d), the maximum number of eddies generated in Box2 occurs in May (similar to Box1), whereas the minimum number occurs in March. In January, July, and September, a difference in the range of 10–18 is found between the numbers of CEs and AEs.

Ordinarily, the NWPO mesoscale eddy characteristics have significant interannual and annual changes consistent with EKE variations (baroclinic instability) caused by the seasonally varying vertical shear between the STCC and North Equatorial Current (NEC) system (Yang et al., 2013; Qiu et al., 2014; Tang et al., 2019). However, the SST variation can affect the formation of eddies by changing the stratification strength of the upper ocean (Shan et al., 2020). The results obtained by Zu et al. (2016) in the North Pacific are negatively correlated. Meanwhile, Cui et al. (2017) found that the interannual variation of the generated number of the eddy is not directly related to El Niño-Southern Oscillation (ENSO). However, Ding et al. (2018) found in the Northeast Pacific that EKE and eddy occurrence number (EON) have certain spatial and temporal relationships with Pacific Decadal Oscillation (PDO) and North Pacific Gyre Oscillation (NPGO). Also, Box2 is more related to PDO and ENSO than Box1 (not shown); the approach used may be different from the method of calculating EKE and EON (Ding et al., 2020). These results suggest that the mesoscale eddy's role in the NWPO region is still unclear. Therefore, further analysis and verification are required to identify the specific physical mechanism.

4.2 *Eddy lifetime and radius*

The general trend characteristics in Box1 and Box2 are shown in Fig. 6. More eddies exist in Box1 (1 094) than in Box2 (753). The mean eddy radius is larger in Box1 (56 km in Box1 and 51 km in Box2). Eddies in Box2 have a longer lifetime (42 d in Box1 and 48 d in Box2). The numbers of CEs and AEs are 567 and 527 in Box1 and 393 and 360 in Box2, respectively. This indicates that there are 4% more CEs than AEs in both areas. At the surface, 77% CEs and 79% AEs in Box1 and 70% CEs and 74% AEs in Box2 survive less than 14 weeks. Only 6 and 7 CEs and 6 and 7 AEs in Box1 and Box2, respectively, live longer than 21 weeks (Figs 5a and b). For instantaneous eddy radii, 90% CEs and 84% AEs in Box1 and 92% CEs and 93% AEs in Box2 are less than 80 km. Box1 has more large-sized (over 150 km) AEs than CEs, and Box2 has more large-sized CEs than AEs (Figs 6c and d).

The eddy detection method (Section 2.3 presents more details) is applied to the 21-layer velocity field. The eddy radius, lifetime, and standard deviations in Box1 and Box2 are shown in Fig. 7. The CEs and AEs radius and lifetime show the same trend. Specifically, the mean radius of CEs (AEs) is 49.4 km (50.2 km) in Box1. From the surface to 1 000 m, the radius of AEs is always slightly larger than that of CEs, except at a depth of 250–350 m (Fig. 7a). The vertically averaged radiuses of CEs and AEs are

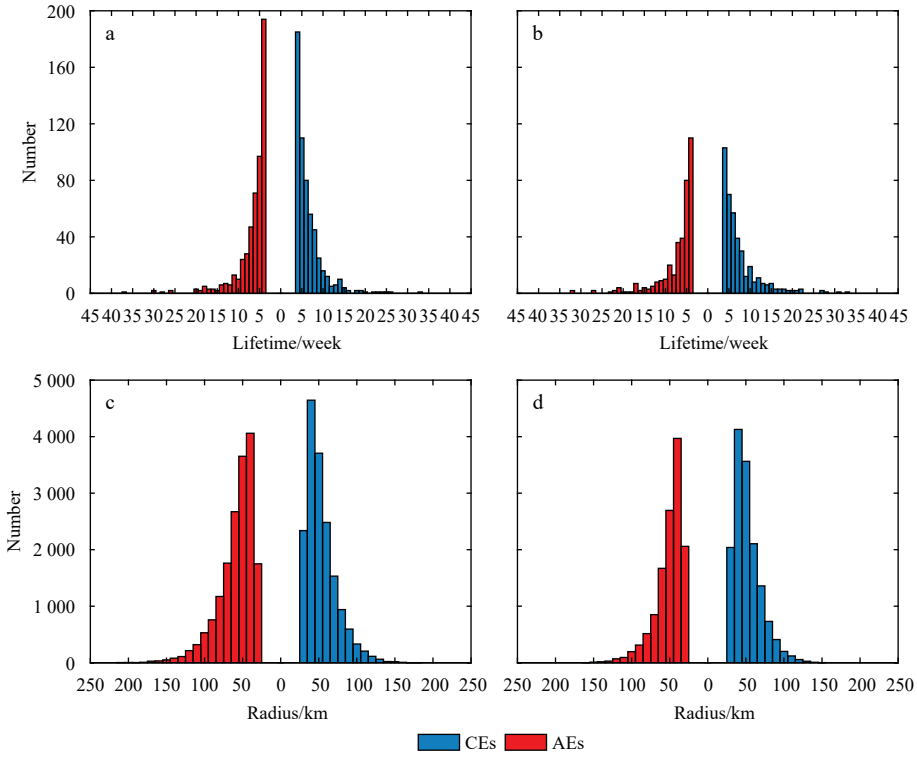

Fig. 6. Histogram of eddy lifetime (a and b) (lifetime>3 weeks) and radius (c and d) (radius>30 km) in Box1 (left panels) and Box2 (right panels).

46.6 km and 46.7 km in Box2, respectively, which are smaller than those in Box1. However, the trend is similar to surface eddies (Fig. 6). With increasing latitude, the eddy radius tends to decrease, which is consistent with the rule of change of Rossby deformation radius. By comparing the standard deviations of eddy radius, the eddies' radiuses in Box1 vary significantly between 500 m and 600 m, and the AEs have a more noticeable difference at the surface. In Box2, the radiuses of AEs vary more than those of CEs between 200 m and 800 m.

Similarly, the eddy lifetime in all 21 layers of Box1 and Box2

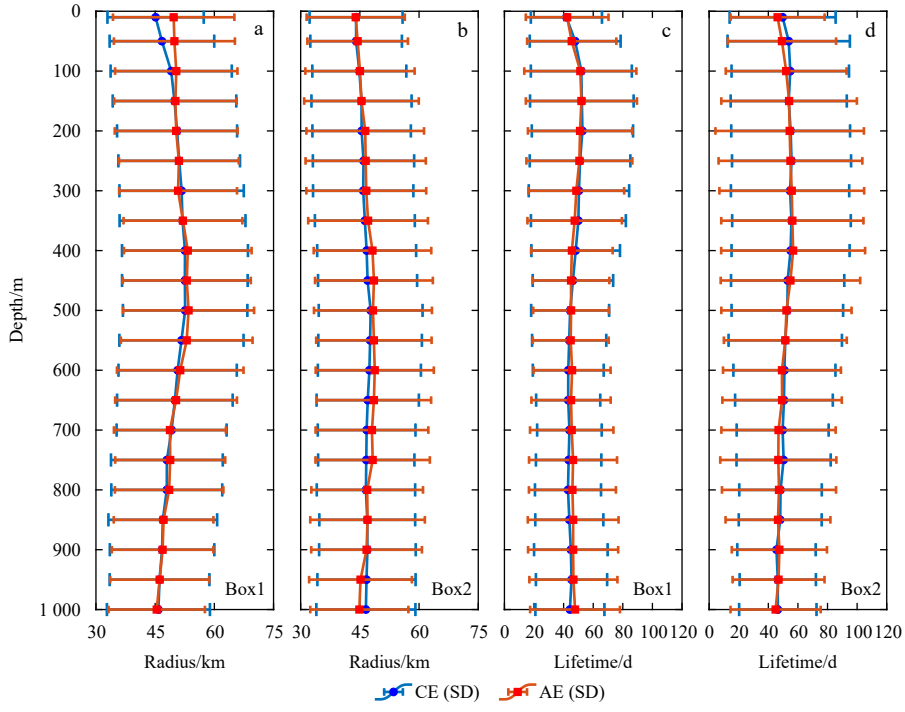

Fig. 7. Vertical profile of mean eddy radius and its standard deviation (SD) in Box1 (a) and Box2 (b) and mean eddy lifetime and its SD in Box1 (c) and Box2 (d).

and their standard deviations are shown in Figs 7c and d. In general, the trend of the vertical lifetime is similar to that at the surface. Eddies in Box1 have shorter lifetimes than those in Box2. The vertically averaged lifetimes of CEs and AEs are about 45 d and 46 d, respectively, in Box1 (Fig. 7c). The AEs have a longer lifetime of up to 3 days at all depths, except between 50 m and 450 m. The vertically averaged lifetimes of CEs and AEs in Box2 are about 50 d and 49 d, respectively, The maximum difference between the lifetimes of CEs and AEs is 5 d at 50 m (Fig. 7d).

Table 1 shows that the number of eddies in Box1 increases from 10 m to 100 m and then decreases until 500 m before increasing again at 1 000 m. In addition, the number of AEs is more than that of CEs at 1 000 m, and the maximum difference is 115. In Box2, the number of eddies first increases from 10 m to 100 m and then decreases until 1 000 m. CEs are more than AEs, and the average difference is 30.

4.3 *Vertical statistics*

In Box1, more CEs are generated than AEs at above 650 m, whereas the opposite trend is observed at below 650 m (Fig. 8a). The numbers of surface CEs and AEs are 567 and 527, respectively. At 50 m, CEs and AEs increase by 149 and 141, respectively. In addition, a minimum difference exists between CEs and AEs at 650 m, and a maximum difference exists at 950 m. In Box2, the number of CEs is always greater than that of AEs, with 393 and 360 surface CEs and AEs, respectively. At 50 m, CEs and AEs increase by 47 and 75, respectively. The number of eddies decreases with depth (Fig. 8b). A minimum difference between CEs and AEs is found at 50 m, and a maximum difference is found at 450 m. The number of vertical eddies in Box1 and Box2 is significantly higher in the subsurface layer, which could differ from surface eddies, because subsurface eddies have weak signals and cannot be detected by satellite altimeter data (Chaigneau et al., 2011; Gordon et al., 2017; Nan et al., 2017; Xu et al., 2019). Xu et al. (2019) conducted a systematic statistical analysis of subsurface eddies in the Northwest Pacific Ocean using model data. They found that the subsurface eddies were concentrated in the latitudinal band between 9°N and 17°N, in the Kuroshio extension region, and in the area east of the Ryukyu Islands. Furthermore, most of them are AEs at 400 m depth.

Table 1. Number of eddies at different depths in Box1 and Box2

Depth/m	Number of eddies					
	Box1			Box2		
	AEs	CEs	All	AEs	CEs	All
10	527	567	1 094	360	393	753
100	619	723	1 342	432	465	897
500	633	665	1 298	362	398	760
1 000	787	672	1 459	295	314	609

The 9-year regionally averaged EKE in Box1 and Box2 decrease with depth in the range of 9–532 cm^2/s^2 and 56–1 029 cm^2/s^2, respectively. As shown in Fig. 8c, the average EKE at the surface (10 m) of Box1 is about 405 cm^2/s^2. At 100 m, it is 205 cm^2/s^2, which is only about 1/2 of the surface value, whereas at 200 m, the EKE decreases to 1/5 of the surface EKE. At 1 000 m, it is only about 12 cm^2/s^2. Compared with the vertical EKE variation in Box1, EKE in Box2 is significantly larger and decreases more slowly with depth. This phenomenon is due to the existence of the Kuroshio. The average EKE of Box2 at the surface is about 843 cm^2/s^2 (Fig. 8d), which is twice the surface EKE of Box1. At 250 m,

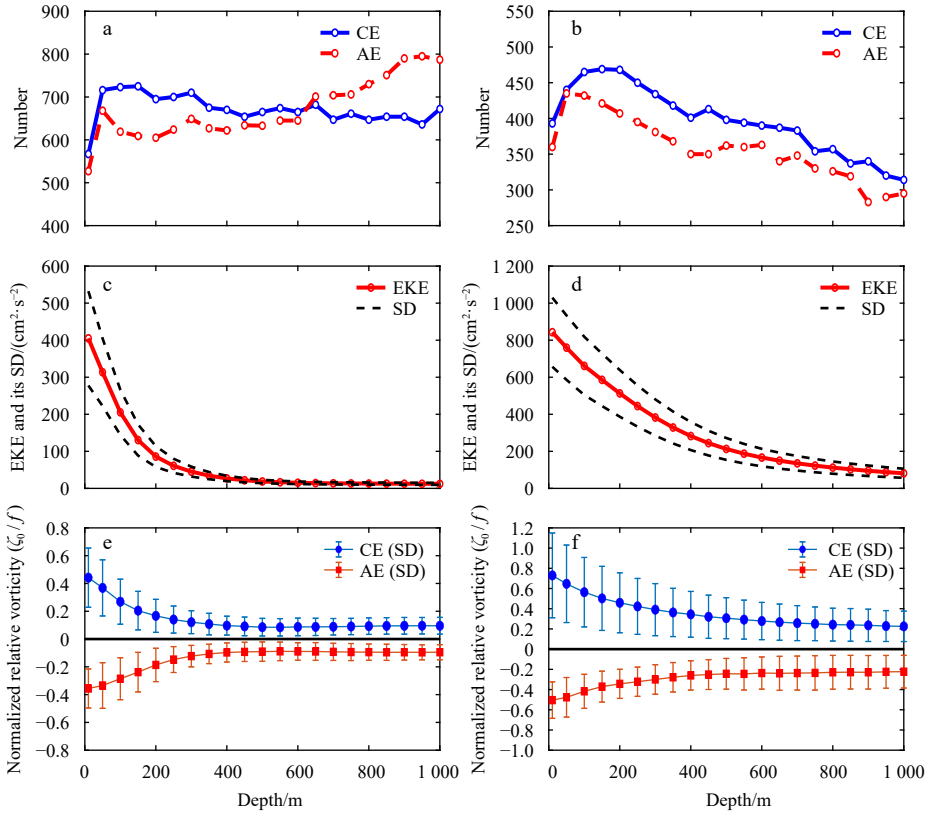

Fig. 8. Vertical distribution of eddy number (a and b), regionally averaged EKE (solid line) and its standard deviation (SD, dashed line) (c and d), and mean normalized relative vorticity (ζ_0/f) and its standard deviation (e and f) in Box1 (left panels) and Box2 (right panels).

this decreases to about 1/2 of the surface EKE, whereas at 600 m, it is about 1/5 of the surface value. At 1 000 m, it is only about 81 cm^2/s^2. These values correspond to the EKE distribution in the two boxes (Fig. 4a).

The normalized relative vorticity (ζ_0/f) is calculated as the maximum relative vorticity ζ_0 divided by the local Coriolis parameter f. Figures 8e and f show that the normalized relative vorticity varies with depth. In Box1, the mean normalized relative vorticity of CEs ranges between 0.10 and 0.44, whereas the values for AEs are between 0.10 and 0.36. At the surface, the mean normalized relative vorticity of CEs (0.44) is larger than that of AEs (0.36). Similar to the vertical distribution of EKE (Figs 8c and d), the mean normalized relative vorticity in Box2 is larger than that in Box1. At the surface, the CEs' mean normalized relative vorticity is 0.73, which is larger than the 0.50 of AEs. This finding can indicate that CEs are more dominant (Fig. 8b). The standard deviations in Figs 8e and f show the great variation of the mean normalized relative vorticity in Box1 and Box2 in the upper ocean (300 m). The attenuation trend of the average normalized relative vorticity is consistent with the respective EKE trends. Higher mean EKE and relative vorticity provide more energy to eddies, which is also why the average eddy lifetime in Box2 is greater than that in Box1.

4.4 *Eddy movement characteristics*

Eddy movements are affected by the β-effect and the background flow field. To study in greater detail how the trajectory, direction, and movement of the NWPO eddies change over time, we select the trajectory of the eddies with a lifetime longer than 21 weeks at 100 m depth in Box1 and Box2 (Figs 9a and b). Most of the CEs and AEs in Box1 are generated in the east and propagate westward before decaying when they reach the western boundary. Only a few of them move with the Kuroshio and survive for a while after reaching the source area of the Kuroshio. A few CEs and AEs are also generated in the southeastern waters of the Taiwan Island, but their propagation range is limited to that region. With increasing latitude, Box2 eddies move to the west. When they reach the western boundary, they turn under the influence of the Kuroshio and topography. There is a CE in Box2 that moves with the Kuroshio Current, and an AE is hovering in the Kuroshio extension area.

The mean velocities of eddy propagation in Box1 and Box2 vary with longitude (Figs 9c and d) and latitude (Figs 9e and f). Most of these long-lived eddies move westward and northward. According to Fig. 9c, the Box1 eddies indicate that meridional velocity changes slightly (less than 1 cm^2/s^2) between 124°E and 145°E. Between 122°E and 124°E, the eddies move sharply north-

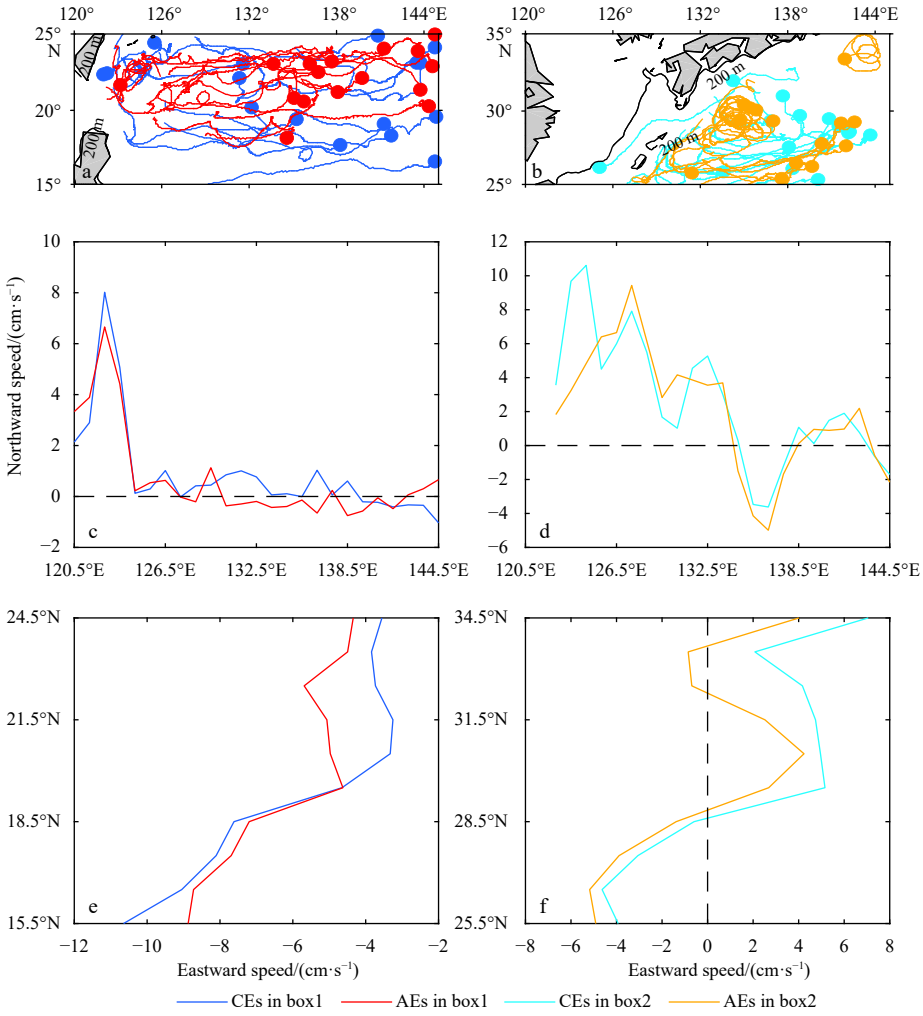

Fig. 9. Eddy trajectories at 100 m depth (a and b), zonal propagation velocity (c and d), and meridional propagation velocity (e and f) of eddies with lifetime >21 weeks and radius >40 km in Box1 (left panels) and Box2 (right panels) . The positive values are north and east. The dotted vertical line is the zero value line.

ward, and the CEs velocity can reach up to 8 cm^2/s^2. The AEs also move at a speed of 6 cm^2/s^2, which is related to the Kuroshio Current flowing northward east of Luzon Island. However, the eddies in Box2 (Fig. 9d) propagate northward, except in the Kuroshio extension between 134°E and 138°E and east of 143°E where they move southward. The velocity of the CEs between 123°E and 124°E can reach about 10 cm^2/s^2. From the perspective of meridional distribution, the average velocity in Box1 is negative (Fig. 9e), which means that the eddy is moving westward at a velocity of about 3–10 cm^2/s^2. The velocity of CEs is greater than that of AEs in the range of 15°–19°N. From 19°N to about 28°N, the speed of AEs is greater than that of CEs. However, north of 28°N, the eddies move eastward with speeds in the range of 4–6 cm^2/s^2. Some AEs move westward between 32°N and 33°N. (Fig. 9f). This finding is roughly consistent with that of Cui et al. (2017).

Overall, eddies in different regions have different characteristic structures. Eddies in Box1 have a shorter lifetime, larger radius, and smaller energy, whereas the opposite is observed in Box2. In addition, the energy and intensity of the eddies in Box1 decay faster with increasing depth of the eddies. At south of 25°N, the eddies propagate westward with a speed of up to 10 cm/s^2. North of 25°N away from the Kuroshio, eddies still move westward. Along the Kuroshio, the eddies begin to change direction and spread eastward.

5 3D features of eddies

5.1 *3D types of eddies*

Based on the 3D eddy detection method (Section 2.3.2), eddies are divided into three types and analyzed at depths of 300 m, 500 m, 700 m, and 1 000 m. A total of 79 693 eddies are detected from 2000 to 2008 in Box1 (44 471) and Box2 (35 222) (Fig. 10). Most of the eddies (68.6%) affect depth above 300 m. Petersen et al. (2013) found that the global number of surface eddies differs by one order of magnitude from the number of eddies at 1 000 m depth. According to the four levels considered in Box1 and Box2, 77.4% of the eddies in Box1 are above 300 m, but only 8.0% reach 1 000 m depth. In Box2, only 57.5% of the eddies are above 300 m, and 27.4% reach 1 000 m. The eddies are grouped into three types, according to the categorization proposed by Dong et al. (2012) and Lin et al. (2015), as follows: bowl-, cone-, and lens-shaped. Yuan et al. (2021) obtained four eddy 3D structures using a 3D eddy identification and tracking algorithm based on pressure anomalies. Except for one more cylindrical shape, the other shapes are consistent with our results. Figure 10 shows that most eddies (~87%) above 300 m in Box1 and Box2 are bowl-shaped. This finding is similar to the bowl-shaped structure of most mesoscale eddies observed by Liu et al. (2017b) in the Gulf Stream region with a maximum depth of about 1 800 m. Zhang et al. (2014) also used satellite altimeter data and Argo profile to identify a CE and an AE, both bowl-shaped eddies, and with depths of 1 200–1 500 m. Cone-shaped eddies make up only about 2.7% of the total. Although the proportion of bowl-shaped eddies decreases with increasing depth, they are still dominant. The proportion of cone-shaped eddies gradually increases with depth. The decrease in the number of bowl-shaped eddies with increasing depth is greater in Box1 than in Box2. The number of lens-shaped eddies stays the same in both regions at 300–500 m. Box2's number of cone-shaped eddies increases by about 10%, whereas that of Box1 increases by about 5%. Bowl-shaped eddies, which are only 300 m, consist of more AEs than CEs in Box2. In addition, cone-shaped eddies at 500–700 m consist of more AEs than CEs (Tables 2 and 3).

5.2 *Distribution eddies at 1 000 m*

Based on the results in Section 5.1, we select eddies that reach 1 000 m depth from the three types of eddies and statistically calculate their meridional and zonal distributions (Fig. 11). Fewer eddies exist between 15°N and 25°N; there are more CEs than AEs. With increasing latitude, the number of eddies increases; peaks appear at 30°N and 31°N (Figs 11a–c). This finding can show how eddy intensity increases with increasing latitude (Figs 3 and 4). Figures 11d–f show more eddies on the east side of 135°E than on the west side. This finding shows that with eddies'

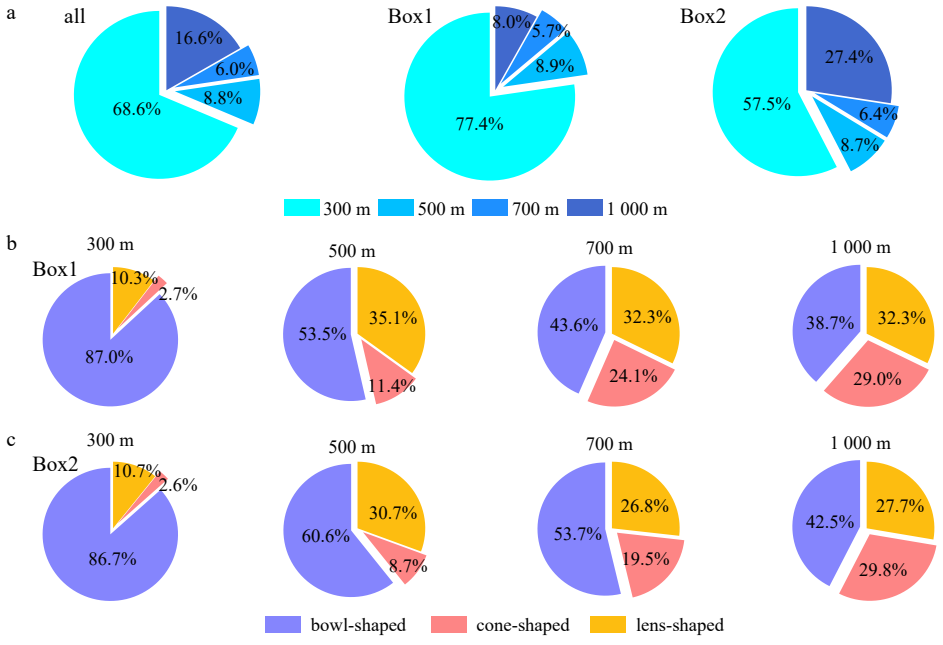

Fig. 10. Pie diagram showing the total instantaneous eddies with a lifetime of more than 3 weeks at 300 m, 500 m, 700 m, and 1 000 m in Box1 and Box2 (a) and the pie charts of the three types of eddies at the corresponding depths in Box1 (b) and Box2 (c).

Table 2. Number of different types of 3D eddies in Box1

Depth/m	Number of eddies					
	Bowl-shaped		Cone-shaped		Lens-shaped	
	CEs	AEs	CEs	AEs	CEs	AEs
300	15 012	14 914	509	402	1 885	1 668
500	1 348	773	251	201	827	562
700	684	424	347	266	477	346
1 000	879	504	662	376	712	442

Table 3. Number of different types of 3D eddies in Box2

Depth/m	Number of eddies					
	Bowl-shaped		Cone-shaped		Lens-shaped	
	CEs	AEs	CEs	AEs	CEs	AEs
300	7 669	9 885	281	246	1 157	1 014
500	998	855	138	128	519	418
700	637	566	210	226	320	280
1 000	2 440	1 675	1 979	901	1 958	722

westward propagation from generation to maturity, their intensity gradually increases. The number of eddies reaching 1 000 m depth is largest between 135°E and 140°E. Then, the intensity of the eddies gradually decreases as they reach the western boundary, where the number of eddies with 1 000 m depth gradually decreases until zero eddies are left. At the same time, the number of CEs of the three types is generally larger than that of AEs. However, at 137°E, the number of bowl-shaped AEs is larger than that of bowl-shaped CEs. The eddy characteristics have noticeable regional features.

5.3 *3D structure cases of the three types of eddies*

Studying the 3D structure is important to better elucidate the characteristics of mesoscale eddies. Three types of CEs and AEs reaching 1 000 m are selected, and six eddies are analyzed. Their sea surface positions are shown in Fig. 12. Their positions are in line with the eddy concentrated area (Fig. 11). Detailed vertical and horizontal sections of temperature, salinity, and velocity are analyzed to better elucidate the 3D structure of the three types of CEs and AEs.

Figures 13a and e show the temperature anomaly of two bowl-shaped eddies (b-1 and b-2) at depths of 10 m, 200 m, 400 m, 600 m, 800 m, and 1 000 m. In Fig. 13a, an obvious cold-core structure appears from 10 m to 1 000 m, indicating that b-1 has a stable eddy structure. The maximum temperature anomaly is 8°C , especially at above 400 m. Hu et al. (2011) used CTD, ADCP, and satellite altimeter data to observe a bowl-like cold eddy in the southwestern part of the South China Sea. The eddy can reach a depth of 500 m. However, the eddy core is more evident at a depth of 50–100 m. Figures 13b–d are the zonal sections corresponding to temperature, salinity, and velocity across the eddy center. The temperature profile has a pronounced and strong upward curvature. The 18°C isotherm, which is considered the thermocline depth, is at the sea surface near the eddy center and at a depth of about 250 m at the edge of the eddy (Fig. 13b). The salinity profile shows a similar structure. Moreover, an obvious low salinity water mass exists at 600 m (Fig. 13c). The velocity profile (speed direction: north is positive and south is negative) shows the connection between the eddy structure and radius (Fig. 13d). The tangential velocity reaches a maximum of 2.0 m/s with a tangential velocity of 0.4 m/s at 800 m. The horizontal temperature anomaly profile (Fig. 13e) shows that b-2 has a warm core with a large temperature anomaly at 200 m. The warm core structure gradually disappears at below 400 m. The temperature profile (Fig. 13f) shows that the isotherm of b-2 significantly drops at its center. If the depth of the 20°C isotherm is taken as the thermocline depth, then the 20°C isotherm reaches about 250 m at the eddy center and about 150 m at the eddy edges. The eddy causes a thermocline drop of nearly 100 m. The salinity profile has the same downward trend as the temperature (Fig. 13g). The velocity profile (Fig. 13h) shows that the maximum tangential velocity of b-2 reaches 0.9 m/s. A comparison of the velocity profiles of b-1 and b-2 shows that the tangential velocity has a clear convergence with a very noticeable bowl-shaped structure.

Figures 14a and e show the horizontal temperature anomaly

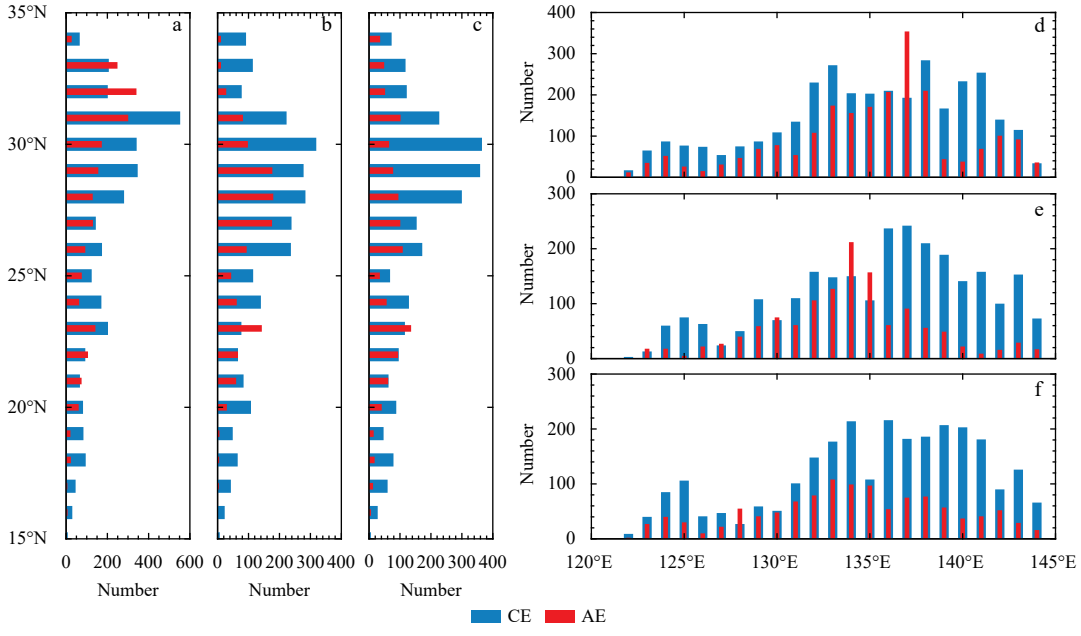

Fig. 11. Meridional (a, b, and c) and zonal (d, e, and f) distributions of the bowl-(a and d), cone-(b and e), and lens-shaped (c and f) eddies at 1 000 m.

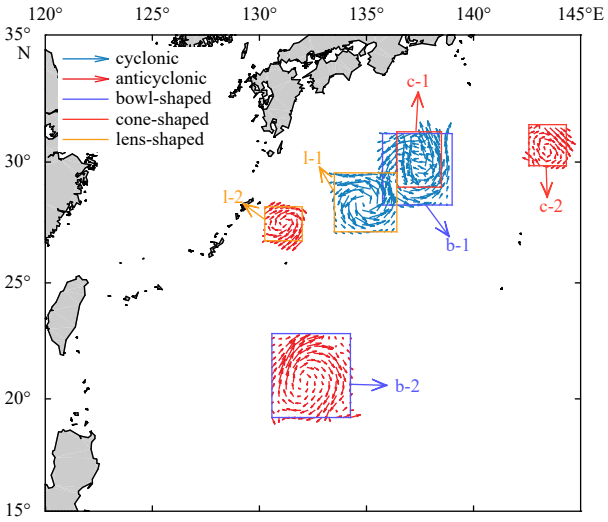

Fig. 12. Location of the six eddy cases. Blue and red arrows are cyclonic and anticyclonic eddies, respectively. The eddy inside the purple frame is bowl-shaped (b-1 and b-2), the red frame is cone-shaped (c-1 and c-2), and the orange frame is lens-shaped (l-1 and l-2). The velocity arrow only represents the direction of the flow field.

profiles of cone-shaped eddies c-1 and c-2. The cold-core structure of c-1 in Fig. 14a is closely related with the flow field. The cold-core gradually becomes larger from top to bottom due to the shape of the eddy. The corresponding temperature profile is convex (Fig. 14b). If the 20°C isotherm depth is taken as the thermocline depth, then the 20°C isotherm rises from 150 m to 50 m at the eddy center. The salinity profile (Fig. 14c) shows that the eddy penetrates the halocline at about 200 m and forms an independent water mass of high salinity in the eddy center. The horizontal temperature anomaly structure of c-2 is unclear (Fig. 14e). However, the vertical temperature (Fig. 14f) and salinity (Fig. 14g) profiles clearly show that the isoline drops at the eddy center. A comparison of the velocity profiles of c-1 and c-2 (Figs 14d and h) shows that the tangential velocity profile differs from that of the bowl-shaped eddies. Furthermore, the cone-shaped eddy radius contour line is consistent with the tangential velocity; it shows a shape with a small top and a large bottom.

The horizontal temperature structure of the lens-shaped eddy l-1 is the same as that of the bowl- and cone-shaped eddies with obvious cold-core structures (Fig. 15a). Corresponding vertical sections of temperature (Fig. 15b) and salinity (Fig. 15c) show that the eddy passes through the thermocline just like the cone-shaped eddy and does not reach the sea surface like a bowl-shaped eddy. Similarly, Fig. 15e shows that the temperature anomaly signal of the lens-shaped eddy l-2 is not very obvious at the surface. The corresponding vertical temperature profile (Fig. 15f) shows that the eddy warm core is at 200 m near the subsurface layer. The velocity profile is the most significant. Similar to the other two types of eddies, the eddy radius contour line coincides with the tangential velocity. In particular, the maximum tangential velocity of l-2 is at a depth of 300 m, which gives l-2 a perfect lens-shaped structure (Fig. 15h).

In general, most eddies (68.6%) are concentrated in the upper ocean at a depth of about 300 m. The bowl-shaped eddies are the dominant type, followed by lens- and cone-shaped eddies. Lin et al. (2015) pointed out that the bowl-shaped eddy is generated by the sea surface wind stress curl, whereas the cone-shaped eddy with a small top and a large bottom is related to the bottom topography and friction. The lens-shaped eddy is generated by the interaction between the flow field and the continental shelf slope. The three types of eddies in different regions have different distributions at different depths. In the latitudinal direction, eddy structure is more stable, and the depth of influence is deeper when the eddies reach the mature stage. In the three types of eddies, the eddy structure of CEs is very obvious. The eddy cores are concentrated between 200 m and 400 m. The structure of AEs is not very obvious, especially the cone-shaped types. The eddy

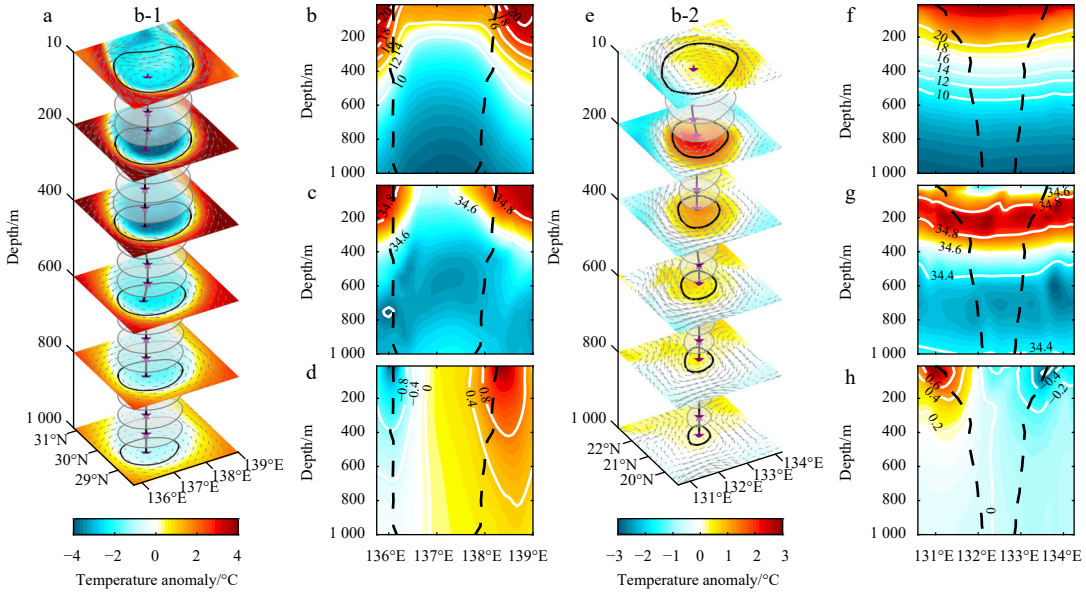

Fig. 13. 3D structure of two 1 000 m bowl-shaped eddies. a. 3D structure of b-1 eddy; b–d. temperature, salinity, and velocity (unit: m/s) profiles of b-1 eddy; e. 3D structure of b-2 eddy; f–h. temperature, salinity, velocity (unit: m/s) profiles b-2 eddy. The solid black line is the eddy contour line, and the black dashed line is the corresponding radius. The arrows only represent the direction of the flow field.

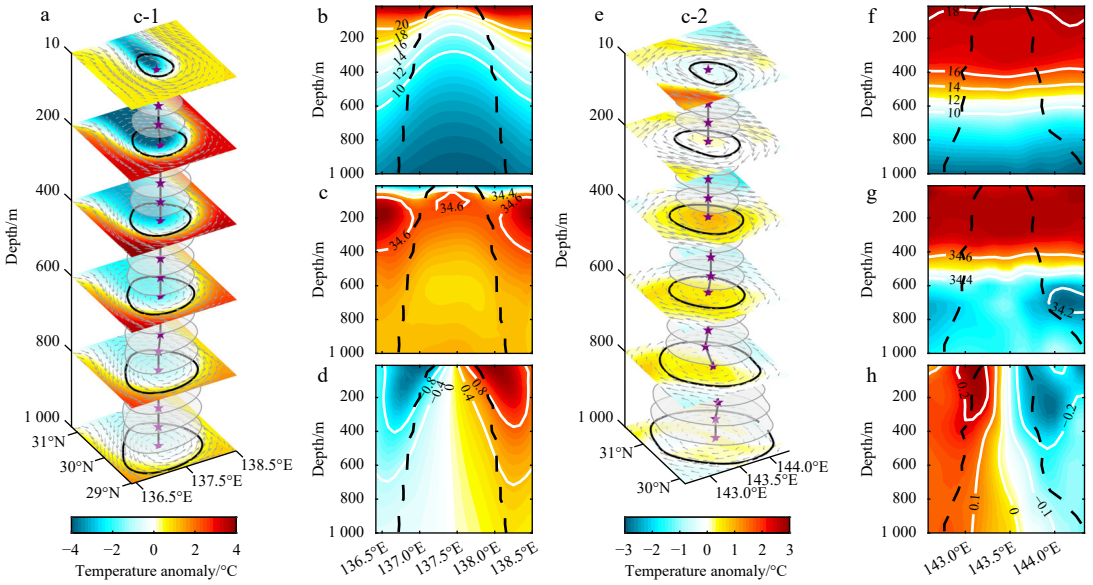

Fig. 14. 3D structure of two 1 000 m cone-shaped eddies. a. 3D structure of c-1 eddy, b–d. temperature, salinity, velocity (unit: m/s) profiles of c-1 eddy; e. 3D structure of c-2 eddy, f–h. temperature, salinity, velocity (unit: m/s) profiles of c-2 eddy. The solid black line is the eddy contour line, and the black dashed line is the corresponding radius. The arrows only represent the direction of the flow field.

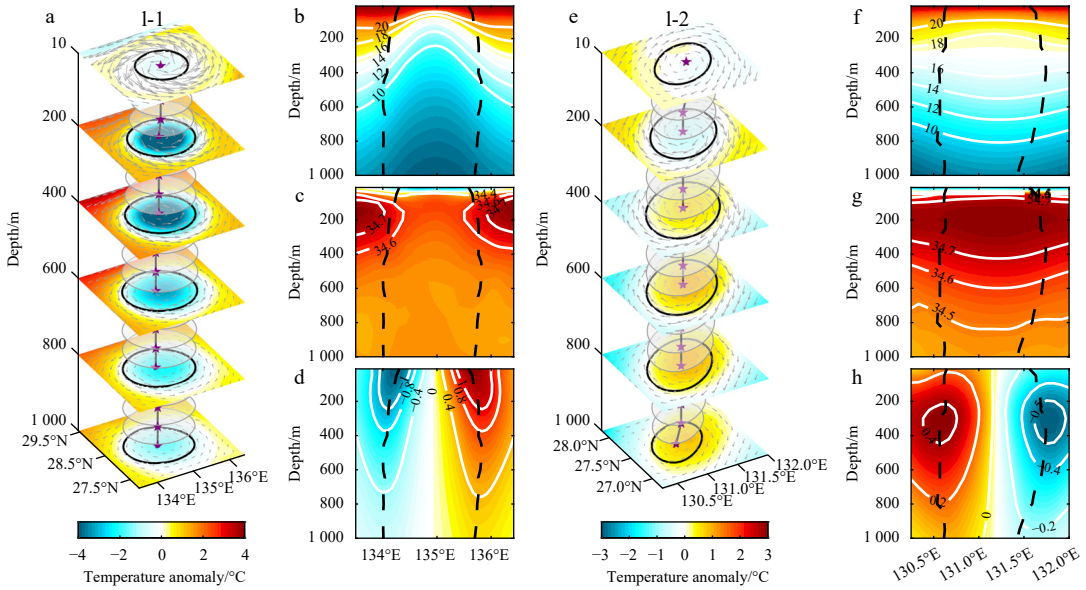

Fig. 15. 3D structure of two 1 000 m lens-shaped eddies. a. 3D structure of l-1 eddy, b–d. temperature, salinity, velocity (unit: m/s) profiles of l-2 eddy; e. 3D structure of l-2 eddy, f–h. temperature, salinity velocity (unit: m/s) profilesof l-2 eddy. The solid black line is the eddy contour line, and the black dashed line is the corresponding radius. The arrows only represent the direction of the flow field.

structure is highly consistent with the flow field. Zhang et al. (2016) and Yang et al. (2020) used observation data, theoretical analysis, and numerical model experiments to observe the vertical tilt of the eddy. In our case, we can also see similar shapes, but the tilt at 0–1 000 m is not as obvious as the tilt at 1 000–2 000 m.

6 Summary and conclusions

The 3D characteristics of mesoscale eddies in the NWPO are analyzed from 9 years of high-resolution numerical model ROMS output. Using an automated eddy detection method, a 21-layer vertical and horizontal 3D eddy dataset is obtained. The dataset includes eddy position, lifetime, size, vorticity, velocity, and energy. A total of 963 CEs and 913 AEs with a lifetime of more than 3 weeks and a radius of more than 30 km are identified. More eddies exist in Box1 (1 094) than in Box2 (753). There are 567 CEs and 527 AEs in Box1 and 393 CEs and 360 AEs in Box2. The interannual variation of Box1 eddies is small; 121 eddies are generated annually on average. The seasonal variation shows that the maximum and minimum numbers of eddies occur in spring (344) and winter (233), respectively. The highest (134) and lowest (57) numbers of eddies are generated in May and November, respectively. Compared with Box1, the interannual variation of

Box2 eddies is pronounced, with strong and weak years. The seasonal variation is larger in spring and autumn than in summer and winter. The number of eddies in May reaches 85 (the highest), whereas the number of eddies in March is 45.

The eddy lifetimes in Box1 and Box2 are generally 4–7 weeks with a radius in the range of 40–50 km. In addition, the eddies in Box2 have a larger radius (56 km in Box1 and 51 km in Box2), but Box2 eddies have a longer lifetime (42 d in Box1 and 48 d in Box2). The average lifetimes of CEs and AEs at the surface in Box1 are 41.9 d and 42.4 d, respectively, with a range of 22–251 d. The average lifetime of CEs and AEs in Box2 is 49.7 d and 46.3 d, respectively, with a range of 22–384 d. Most eddies (90%) have a radius of less than 80 km, and 75% have a lifetime of fewer than 14 weeks. The mean vertical radius (lifetime) is 49.8 km (45.5 d) in Box1, and this is 46.6 km (49.5 d) in Box2. The 9-year regional average EKE of Box1 and Box2 are 9–532 cm^2/s^2 and 56–1 029 cm^2/s^2, respectively. The relative vorticity of Box1 CEs is between 0.10 and 0.44, and that of AEs is between 0.10 and 0.36. The relative vorticity of CEs in Box2 is in the range of 0.23–0.73, and that of AEs is in the range of 0.22–0.55. Influenced by the β-effect, the eddies propagate westward at latitudes less than 28°N and reach a maximum velocity of 11cm/s at about 15°N in the NWPO. The velocity of CEs between 15°N and 19°N is greater than that of AEs, and the propagation direction of the eddies changes on the northern and southern sides of 28°N. The different statistical characteristics of Box1 and Box2 eddies are due to the differences in latitude and circulation structure.

Most eddies (68.6%) are concentrated in the upper ocean (about 300 m in depth). Only 16.6% of the eddies extend to 1 000 m. Bowl-shaped eddies (~87%) are the main type, followed by lens-shaped (~10%) and cone-shaped ones (~3%). The uplifting effect of CEs on the thermocline is very obvious, especially in cone- and lens-shaped CEs. The distribution characteristics of temperature and salinity in CEs are related to their 3D structure. However, the distribution characteristics in AEs are different, especially for cone-shaped eddies. This finding may be due to the strong current field at the surface layer, which compresses the eddy and makes the surface shape and structure smaller. The temperature and salinity changes at depths above 400 m are not evident. With increasing depth, the current weakens, allowing the eddy shape to become larger and the eddy structure to gradually become obvious.

At present, only a few mesoscale eddy field observations exist, and altimeter data can only reveal the surface characteristics of eddies. At middle and low latitudes, the SST and salinity signals in eddies are weak, and chlorophyll observation data are scarce. These cannot be used to study the 3D characteristics of eddies. Although the results in this paper are purely based on model data and there is a lack of validation from *in situ* observational data, these results can also be used to supplement more eddy field observations in the future. Therefore, 3D eddy properties obtained from model outputs represent a more economical and quick method for studying these characteristics.

Acknowledgements

The authors thank AVISO+ (http://www.aviso.altimetry.fr/) for providing the SSHA data and mesoscale eddy trajectory atlas product. The altimetric Mesoscale Eddy Trajectories Atlas (META2.0) was produced by SSALTO/DUACS and distributed by AVISO+ with support from CNES, in collaboration with Oregon State University with support from NASA. The SST products used in this study are distributed by CMEMS (http://marine.copernicus.eu/).

References

Aguedjou H M A, Dadou I, Chaigneau A, et al. 2019. Eddies in the tropical Atlantic Ocean and their seasonal variability. Geophysical Research Letters, 46(21): 12156–12164, doi: 10.1029/2019GL083925

Amante C, Eakins B W. 2009. ETOPO1 arc-minute global relief model: procedures, data sources and analysis. NOAA Technical Memorandum NESDIS NGDC-24, National Geophysical Data Center, NOAA

Chaigneau A, Eldin G, Dewitte B. 2009. Eddy activity in the four major upwelling systems from satellite altimetry (1992–2007). Progress in Oceanography, 83(1–4): 117–123, doi: 10.1016/j.pocean.2009.07.012

Chaigneau A, Le Texier M, Eldin G, et al. 2011. Vertical structure of mesoscale eddies in the eastern South Pacific Ocean: A composite analysis from altimetry and Argo profiling floats. Journal of Geophysical Research: Oceans, 116(C11): C11025

Chapman D C. 1985. Numerical treatment of cross-shelf open boundaries in a barotropic coastal ocean model. Journal of Physical Oceanography, 15(8): 1060–1075, doi: 10.1175/1520-0485(1985)015<1060:NTOCSO>2.0.CO;2

Chassignet E P, Yeager S G, Fox-Kemper B, et al. 2020. Impact of horizontal resolution on global ocean-sea ice model simulations based on the experimental protocols of the Ocean Model Intercomparison Project phase 2 (OMIP-2). Geoscientific Model Development, 13(9): 4595–4637, doi: 10.5194/gmd-13-4595-2020

Chelton D B, Gaube P, Schlax M G, et al. 2011a. The influence of nonlinear mesoscale eddies on near-surface oceanic chlorophyll. Science, 334(6054): 328–332, doi: 10.1126/science.1208897

Chelton D B, Schlax M G, Samelson R M. 2011b. Global observations of nonlinear mesoscale eddies. Progress in Oceanography, 91(2): 167–216, doi: 10.1016/j.pocean.2011.01.002

Chen Genxin, Hou Yijun, Chu Xiaoqing. 2011. Mesoscale eddies in the South China Sea: Mean properties, spatiotemporal variability, and impact on thermohaline structure. Journal of Geophysical Research: Oceans, 116(C6): C06018

Cheng Y H, Ho C R, Zheng Quanan, et al. 2017. Statistical features of eddies approaching the Kuroshio east of Taiwan Island and Luzon Island. Journal of Oceanography, 73(4): 427–438, doi: 10.1007/s10872-017-0411-7

Chern C S, Wang J, Wang Dongping. 1990. The exchange of Kuroshio and East China Sea shelf water. Journal of Geophysical Research: Oceans, 95(C9): 16017–16023, doi: 10.1029/JC095iC09p16017

Cui Wei, Wang Wei, Ma Yi, et al. 2017. Identification and analysis of mesoscale eddies in the northwestern Pacific Ocean from 1993–2014 based on altimetry data. Haiyang Xuebao (in Chinese), 39(2): 16–28

Dai Jun, Wang Huizan, Zhang Weimin, et al. 2020. Observed spatiotemporal variation of three-dimensional structure and heat/salt transport of anticyclonic mesoscale eddy in Northwest Pacific. Journal of Oceanology and Limnology, 38(6): 1654–1675, doi: 10.1007/s00343-019-9148-z

de Marez C, L'Hégare T P, Morvan M, et al. 2019. On the 3D structure of eddies in the Arabian Sea. Deep-Sea Research Part I: Oceanographic Research Papers, 150: 103057, doi: 10.1016/j.dsr.2019.06.003

Ding Mengrong, Lin Pengfei, Liu Hailong, et al. 2018. Increased eddy activity in the northeastern Pacific during 1993–2011. Journal of Climate, 31(1): 387–399, doi: 10.1175/JCLI-D-17-0309.1

Ding Mengrong, Lin Pengfei, Liu Hailong, et al. 2020. Lagrangian eddy kinetic energy of ocean mesoscale eddies and its application to the northwestern Pacific. Scientific Reports, 10: 12791, doi: 10.1038/s41598-020-69503-z

Dong Di, Brandt P, Chang Ping, et al. 2017. Mesoscale eddies in the northwestern Pacific Ocean: Three-dimensional eddy structures and heat/salt transports. Journal of Geophysical Research: Oceans, 122(12): 9795–9813

Dong Changming, Lin Xiayan, Liu Yu, et al. 2012. Three-dimensional oceanic eddy analysis in the Southern California Bight from a numerical product. Journal of Geophysical Research: Oceans,

117(C7): C00H14
Dong Changming, McWilliams J C, Liu Yu, et al. 2014. Global heat and salt transports by eddy movement. Nature Communications, 5: 3294, doi: 10.1038/ncomms4294
Gordon A L. 1986. Interocean exchange of thermocline water. Journal of Geophysical Research: Oceans, 91(C4): 5037–5046, doi: 10.1029/JC091iC04p05037
Gordon A L, Shroyer E, Murty V S N. 2017. An Intrathermocline eddy and a tropical cyclone in the Bay of Bengal. Scientific Reports, 7: 46218, doi: 10.1038/srep46218
Hasunuma K, Yoshida K. 1978. Splitting of the subtropical gyre in the western North Pacific. Journal of Oceanography, 34(4): 160–172, doi: 10.1007/BF02108654
He Zhongjie. 2007. Study of mesoscale eddies in the subtropical ocean of the Northwest-Pacific and adjacent area (in Chinese) [dissertation]. Qingdao: Ocean University of China
Hu Jianyu, Gan Jianping, Sun Zhenyu, et al. 2011. Observed three-dimensional structure of a cold eddy in the southwestern South China Sea. Journal of Geophysical Research: Oceans, 116(C5): C05016
Hu Dunxin, Wu Lixin, Cai Wenju, et al. 2015. Pacific western boundary currents and their roles in climate. Nature, 522(7556): 299–308, doi: 10.1038/nature14504
Ji Jinlin, Dong Changming, Zhang Biao, et al. 2018. Oceanic eddy characteristics and generation mechanisms in the Kuroshio Extension region. Journal of Geophysical Research: Oceans, 123(11): 8548–8567, doi: 10.1029/2018JC014196
Jing Zhiyou, Fox-Kemper B, Cao Haijin, et al. 2021. Submesoscale fronts and their dynamical processes associated with symmetric instability in the Northwest Pacific Subtropical Ocean. Journal of Physical Oceanography, 51(1): 83–100, doi: 10.1175/JPO-D-20-0076.1
Kang Lin, Wang Fan, Chen Yongli. 2010. Eddy generation and evolution in the North Pacific Subtropical Countercurrent (NPSC) zone. Chinese Journal of Oceanology and Limnology, 28(5): 968–973, doi: 10.1007/s00343-010-9010-9
Lin Pengfei. 2005. Statistical analyses on mesoscale eddies in the South China Sea and the Northwest Pacific (in Chinese)[dissertation]. Qingdao: Institute of Oceanology, Chinese Academy of Sciences
Lin Xiayan, Dong Changming, Chen Dake, et al. 2015. Three-dimensional properties of mesoscale eddies in the South China Sea based on eddy-resolving model output. Deep-Sea Research Part I: Oceanographic Research Papers, 99: 46–64
Lin Xiayan, Guan Yuping, Liu Yu. 2013. Three-dimensional structure and evolution process of Dongsha Cold Eddy during autumn 2000. Journal of Tropical Oceanography, 32(2): 55–65
Lin Hongyang, Hu Jianyu, Zheng Quanan. 2012. Satellite altimeter data analysis of the South China Sea and the northwest Pacific Ocean: Statistical features of oceanic mesoscale eddies. Journal of Oceanography in Taiwan Strait, 31(1): 105–113
Lin Pengfei, Liu Hailong, Ma Jing, et al. 2019. Ocean mesoscale structure-induced air-sea interaction in a high-resolution coupled model. Atmospheric and Oceanic Science Letters, 12(2): 98–106, doi: 10.1080/16742834.2019.1569454
Liu Yu, Dong Changming, Guan Yuping, et al. 2012. Eddy analysis in the subtropical zonal band of the North Pacific Ocean. Deep-Sea Research Part I: Oceanographic Research Papers, 68: 54–67, doi: 10.1016/j.dsr.2012.06.001
Liu Yu, Dong Changming, Liu Xiaohui, et al. 2017a. Antisymmetry of oceanic eddies across the Kuroshio over a shelfbreak. Scientific Reports, 7: 6761, doi: 10.1038/s41598-017-07059-1
Liu Li, Silver D, Bemis K, et al. 2017b. Illustrative visualization of mesoscale ocean eddies. Computer Graphics Forum, 36(3): 447–458, doi: 10.1111/cgf.13201
Lukas R, Firing E, Hacker P, et al. 1991. Observations of the Mindanao Current during the western equatorial Pacific Ocean circulation study. Journal of Geophysical Research: Oceans, 96(C4): 7089–7104, doi: 10.1029/91JC00062
Lukas R, Yamagata T, McCreary J P. 1996. Pacific low-latitude western boundary currents and the Indonesian throughflow. Journal of Geophysical Research: Oceans, 101(C5): 12209–12216, doi: 10.1029/96JC01204
Ma Jing, Xu Haiming, Dong Changmimg, et al. 2015. Atmospheric responses to oceanic eddies in the Kuroshio Extension region. Journal of Geophysical Research: Atmospheres, 120(13): 6313–6330
Ma Jing, Xu Haiming, Dong Changming. 2016. Seasonal variations in atmospheric responses to oceanic eddies in the Kuroshio Extension. Tellus A: Dynamic Meteorology and Oceanography, 68(1): 31563, doi: 10.3402/tellusa.v68.31563
McCreary J P Jr, Lu P. 1994. Interaction between the subtropical and equatorial ocean circulations: The subtropical cell. Journal of Physical Oceanography, 24(2): 466–497, doi: 10.1175/1520-0485(1994)024<0466:IBTSAE>2.0.CO;2
McGillicuddy D J Jr, Johnson R, Siegel D A, et al. 1999. Mesoscale variations of biogeochemical properties in the Sargasso Sea. Journal of Geophysical Research: Oceans, 104(C6): 13381–13394, doi: 10.1029/1999JC900021
McNeil J D, Jannasch H W, Dickey T, et al. 1999. New chemical, bio-optical and physical observations of upper ocean response to the passage of a mesoscale eddy off Bermuda. Journal of Geophysical Research: Oceans, 104(C7): 15537–15548, doi: 10.1029/1999JC900137
Meng Yao, Liu Hailong, Ding Ruiqiang, et al. 2021. The predictability limit of ocean mesoscale eddy tracks in the Kuroshio Extension region. Frontiers in Marine Science, 8: 658125, doi: 10.3389/fmars.2021.658125
Nan Feng, Yu Fei, Wei Chuanjie, et al. 2017. Observations of an extra-large subsurface anticyclonic eddy in the northwestern Pacific subtropical gyre. Journal of Marine Science: Research & Development, 7: 234
Nencioli F, Dong Changming, Dickey T, et al. 2010. A vector geometry-based eddy detection algorithm and its application to a high-resolution numerical model product and high-frequency radar surface velocities in the Southern California Bight. Journal of Atmospheric and Oceanic Technology, 27(3): 564–579, doi: 10.1175/2009JTECHO725.1
Noh Y, Yim B Y, You S H, et al. 2007. Seasonal variation of eddy kinetic energy of the North Pacific Subtropical Countercurrent simulated by an eddy-resolving OGCM. Geophysical Research Letters, 34(7): L07601
Okubo A. 1970. Horizontal dispersion of floatable particles in the vicinity of velocity singularities such as convergences. Deep-Sea Research and Oceanographic Abstracts, 17(3): 445–454, doi: 10.1016/0011-7471(70)90059-8
Orlanski I. 1976. A simple boundary condition for unbounded hyperbolic flows. Journal of Computational Physics, 21(3): 251–269
Petersen M R, Williams S J, Maltrud M E, et al. 2013. A three-dimensional eddy census of a high-resolution global ocean simulation. Journal of Geophysical Research: Oceans, 118(4): 1759–1774, doi: 10.1002/jgrc.20155
Qiu Bo. 1999. Seasonal eddy field modulation of the North Pacific Subtropical Countercurrent: TOPEX/Poseidon observations and theory. Journal of Physical Oceanography, 29(10): 2471–2486
Qiu Bo, Chen Shuiming. 2005. Eddy-induced heat transport in the subtropical North Pacific from Argo, TMI, and altimetry measurements. Journal of Physical Oceanography, 35(4): 458–473, doi: 10.1175/JPO2696.1
Qiu Bo, Chen Shuiming. 2010. Interannual variability of the North Pacific Subtropical Countercurrent and its associated mesoscale eddy field. Journal of Physical Oceanography, 40(1): 213–225, doi: 10.1175/2009JPO4285.1
Qiu Bo, Chen Shuiming. 2013. Concurrent decadal mesoscale eddy modulations in the western North Pacific subtropical gyre. Journal of Physical Oceanography, 43(2): 344–358, doi: 10.1175/JPO-D-12-0133.1
Qiu Bo, Chen Shuiming, Klein P, et al. 2014. Seasonal mesoscale and submesoscale eddy variability along the North Pacific subtropical countercurrent. Journal of Physical Oceanography, 44(12): 3079–3098

Qiu Bo, Imasato N. 1990. A numerical study on the formation of the Kuroshio Counter Current and the Kuroshio Branch Current in the East China Sea. Continental Shelf Research, 10(2): 165–184, doi: 10.1016/0278-4343(90)90028-K

Qu Tangdong, Mitsudera H, Yamagata T. 1998. On the western boundary currents in the Philippine Sea. Journal of Geophysical Research: Oceans, 103(C4): 7537–7548, doi: 10.1029/98JC00263

Raymond W H, Kuo H L. 1984. A radiation boundary condition for multi-dimensional flows. Quarterly Journal of the Royal Meteorological Society, 110(464): 535–551

Roemmich D, Gilson J. 2001. Eddy transport of heat and thermocline waters in the North Pacific: A key to interannual/decadal climate variability?. Journal of Physical Oceanography, 31(3): 675–687, doi: 10.1175/1520-0485(2001)031<0675:ETOHAT>2.0.CO;2

Sadarjoen I A, Post F H. 2000. Detection, quantification, and tracking of vortices using streamline geometry. Computers & Graphics, 24(3): 333–341

Shan Xuan, Jing Zhao, Gan Bolan, et al. 2020. Surface heat flux induced by mesoscale eddies cools the Kuroshio-Oyashio Extension region. Geophysical Research Letters, 47(1): e2019GL086050

Stammer D. 1998. On eddy characteristics, eddy transports, and mean flow properties. Journal of Physical Oceanography, 28(4): 727–739, doi: 10.1175/1520-0485(1998)028<0727: OECETA>2.0.CO;2

Su Jilan, Li Yan, Wang Qi. 2001. Some important research topics for China in ocean sciences in the early 21st century. Advance in Earth Sciences, 16(5): 658–663

Sun Wenjin, Dong Changming, Tan Wei, et al. 2018. Vertical structure anomalies of oceanic eddies and eddy-induced transports in the South China Sea. Remote Sensing, 10(5): 795, doi: 10.3390/rs10050795

Sun Wenjin, Dong Changming, Wang Ruyun, et al. 2017. Vertical structure anomalies of oceanic eddies in the Kuroshio Extension region. Journal of Geophysical Research: Oceans, 122(2): 1476–1496, doi: 10.1002/2016JC012226

Sun Bowen, Liu Chuanyu, Wang Fan. 2019. Global meridional eddy heat transport inferred from Argo and altimetry observations. Scientific Reports, 9: 1345, doi: 10.1038/s41598-018-38069-2

Tang Bo, Hou Yijun, Yin Yuqi, et al. 2019. Probability distributions of statistical characteristics of mesoscale eddies in the global ocean. International Journal of Remote Sensing, 40(16): 6283–6297, doi: 10.1080/01431161.2019.1590875

Toole J M, Millard R C, Wang Z, et al. 1990. Observations of the Pacific North Equatorial Current bifurcation at the Philippine coast. Journal of Physical Oceanography, 20(2): 307–318, doi: 10.1175/1520-0485(1990)020<0307:OOTPNE>2.0.CO;2

Wang Qingye, Cao Ruixue, Zhang Shuwen, et al. 2009. Bifurcation of pacific north equatorial current at the surface. Science in China Series D: Earth Sciences, 52(2): 227–231, doi: 10.1007/s11430-009-0020-4

Wang Yang, Li Cheng, Liu Qingyu. 2020a. Observation of an anti-cyclonic mesoscale eddy in the subtropical northwestern Pacific Ocean from altimetry and Argo profiling floats. Acta Oceanologica Sinica, 39(7): 79–90, doi: 10.1007/s13131-020-1596-y

Wang Ru, Li Haiyan, Meng Lei. 2019. Mesoscale eddies energy characteristic in the Kuroshio Extension and North Pacific subtropical countercurrent region. Haiyang Xuebao (in Chinese), 41(11): 1–14

Wang Huizan, Liu Ding, Zhang Weimin, et al. 2020b. Characterizing the capability of mesoscale eddies to carry drifters in the northwest Pacific. Journal of Oceanology and Limnology, 38(6): 1711–1728, doi: 10.1007/s00343-019-9149-y

Weiss J. 1991. The dynamics of enstrophy transfer in two-dimensional hydrodynamics. Physica D: Nonlinear Phenomena, 48(2–3): 273–294, doi: 10.1016/0167-2789(91)90088-Q

Wunsch C, Ferrari R. 2004. Vertical mixing, energy, and the general circulation of the oceans. Annual Review of Fluid Mechanics, 36: 281–314, doi: 10.1146/annurev.fluid.36.050802.122121

Xu Anqi, Yu Fei, Nan Feng. 2019. Study of subsurface eddy properties in northwestern Pacific Ocean based on an eddy-resolving OGCM. Ocean Dynamics, 69(4): 463–474, doi: 10.1007/s10236-019-01255-5

Yang Haiyuan, Chang Ping, Qiu Bo, et al. 2019a. Mesoscale air-sea interaction and its role in eddy energy dissipation in the Kuroshio Extension. Journal of Climate, 32(24): 8659–8676, doi: 10.1175/JCLI-D-19-0155.1

Yang Zhibin, Wang Guihua, Chen Changlin. 2019b. Horizontal velocity structure of mesoscale eddies in the South China Sea. Deep-Sea Research Part I: Oceanographic Research Papers, 149: 103055, doi: 10.1016/j.dsr.2019.06.001

Yang Guang, Wang Fan, Li Yuanlong, et al. 2013. Mesoscale eddies in the northwestern subtropical Pacific Ocean: Statistical characteristics and three-dimensional structures. Journal of Geophysical Research: Oceans, 118(4): 1906–1925, doi: 10.1002/jgrc.20164

Yang Shengmu, Xing Jiuxing, Sheng Jinyu, et al. 2020. The impact of the planetary β-effect on the vertical structure of a coherent vortex in the South China Sea. Ocean Dynamics, 70(7): 879–896, doi: 10.1007/s10236-020-01375-3

Yang Xiao, Xu Guangjun, Liu Yu, et al. 2020. Multi-source data analysis of mesoscale eddies and their effects on surface chlorophyll in the bay of bengal. Remote Sensing, 12(21): 3485, doi: 10.3390/rs12213485

Yuan Liming, Tian Fenglin, Xu Suqin, et al. 2021. Three-dimensional mesoscale eddy identification and tracking algorithm based on pressure anomalies. Journal of Oceanology and Limnology, 39(6): 2153–2166, doi: 10.1007/s00343-021-0309-5

Zhang Zhiwei, Li Peiliang, Xu Lixiao, et al. 2015. Subthermocline eddies observed by rapid-sampling Argo floats in the subtropical northwestern Pacific Ocean in Spring 2014. Geophysical Research Letters, 42(15): 6438–6445, doi: 10.1002/2015GL064601

Zhang Zhiwei, Tian Jiwei, Qiu Bo, et al. 2016. Observed 3D structure, generation, and dissipation of oceanic mesoscale eddies in the South China Sea. Scientific Reports, 6: 24349, doi: 10.1038/srep24349

Zhang Zhengguang, Wang Wei, Qiu Bo. 2014. Oceanic mass transport by mesoscale eddies. Science, 345(6194): 322–324, doi: 10.1126/science.1252418

Zhang Zhengguang, Zhang Yu, Wang Wei, et al. 2013. Universal structure of mesoscale eddies in the ocean. Geophysical Research Letters, 40(14): 3677–3681, doi: 10.1002/grl.50736

Zheng Congcong, Yang Yuxing, Wang Faming. 2014. Spatial-temporal features of eddies in the North Pacific. Marine Sciences, 38(10): 105–112

Zhou Hui, Liu Xueqi, Li Ruixiang, et al. 2021. Intraseasonal variability of the north equatorial current bifurcation off the philippines. Journal of Geophysical Research: Oceans, 126(11): e2021JC017646

Zhou Hui, Xu Jianping, Guo Peifang, et al. 2006. A summary on studies of western boundary current system in the North Pacific Ocean. Journal of Marine Sciences, 24(2): 49–59

Zhou Hui, Yuan Dongliang, Guo Peifang, et al. 2010. Meso-scale circulation at the intermediate-depth east of Mindanao observed by Argo profiling floats. Science China Earth Sciences, 53(3): 432–440, doi: 10.1007/s11430-009-0196-7

Zu Yongcan, Fang Yue, Gao Xiaoqian, et al. 2016. Seasonal and interannual variation of mesoscale eddies in the North Pacific Ocean: a statistical analysis. Advances in Marine Science, 34(2): 197–206

Appendix: Model evaluation

SST is among the most important observation indexes for air-sea interaction and climate change. We use OSTIA SST data from 2000 to 2008 to evaluate the model outputs and calculate the seasonal mean SST distribution over the NWPO in summer and winter. As shown in Fig. A1, the simulated regional seasonal SST is similar to the observed one. Both the OSTIA data and the model output show that the summer SST north of 30°N is less than 25°C in the East China Sea. An obvious low-temperature region exists in the Kuroshio extension south of Japan, where the simulated cold tongue area extends southward by about 1°–2°N. In winter, the OSTIA and model results show a very significant temperature gradient along the 200 m isobath, and the modeled temperature gradient is larger at the 200 m isobath. The SST tends to extend to the continental shelf of the East China Sea due to the intrusion of the Kuroshio northeast of the Taiwan Island. The low-temperature zone near the coast of Jiangsu Province in China and the cold tongue outside the Yangtze River estuary are very similar. Some subtle differences can be due to the fact that the model data represent ocean temperature at a depth of 10 m, whereas the OSTIA data are the merged multi-satellite sea skin temperature.

Figure A2 shows the average normalized SST time series for the entire northwestern Pacific from 2000 to 2008. The model results and the OSTIA data show the same trend, and the correlation coefficient between the two is about 0.99. Figure A2a shows that the model temperature is lower than the OSTIA data in winter with a maximum difference of 1.4°C . The normalized EKE time series (Fig. A2b) has a strong seasonal signal similar to SST; it is strongest in summer and weakest in winter. This finding is consistent with the changes in the STCC area reported by Qiu (1999). After a 90-d seasonal Gaussian smoothing, the correlation coefficient between the two is about 0.59, which shows high correlation. The results of the ROMS model have good consistency with the satellite observation data and can thus be used for 3D eddy detection in the NWPO.

To verify the eddy detection results from the model output, we apply the same geometry-based eddy detection algorithm (Nencioli et al., 2010) to AVISO data (Fig. A3). We interpolate the model and AVISO data to (1/8)°×(1/8)° due to their different horizontal resolutions. We calculate the number of eddies by treating the entire eddy lifetime as one eddy. A total of 32 323 eddies are detected in the ROMS data and 24 965 eddies in the AVISO data. The number of eddies detected from the model results is 12.8% more than that from AVISO data (Figs A3a–b). Their mean radius distribution patterns are very similar (Figs A3c–d). However, many eddies from the model data have a lifetime of less than 1 week. For further statistical analysis, threshold screening is performed on the detection results (Fig. A4) with a lifetime longer than 3 weeks and a radius larger than 30 km.

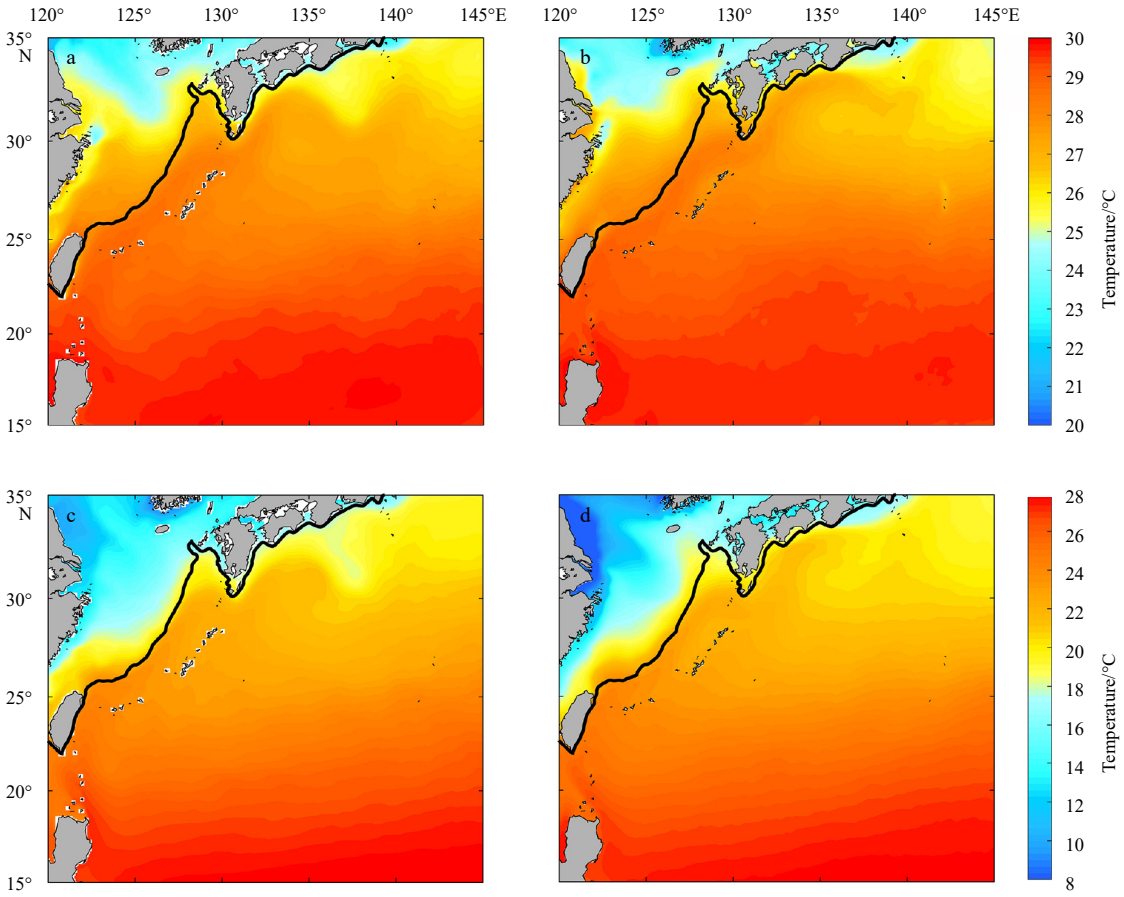

Fig. A1. Seasonal mean SST distribution in summer and winter from 2000 to 2008. a and b. Summer months, June to August (JJA); c and d. winter months, December to February (DJF). The ROMS model results are displayed on the left, and OSTIA data results are on the right. The black line is the 200 m isobath.

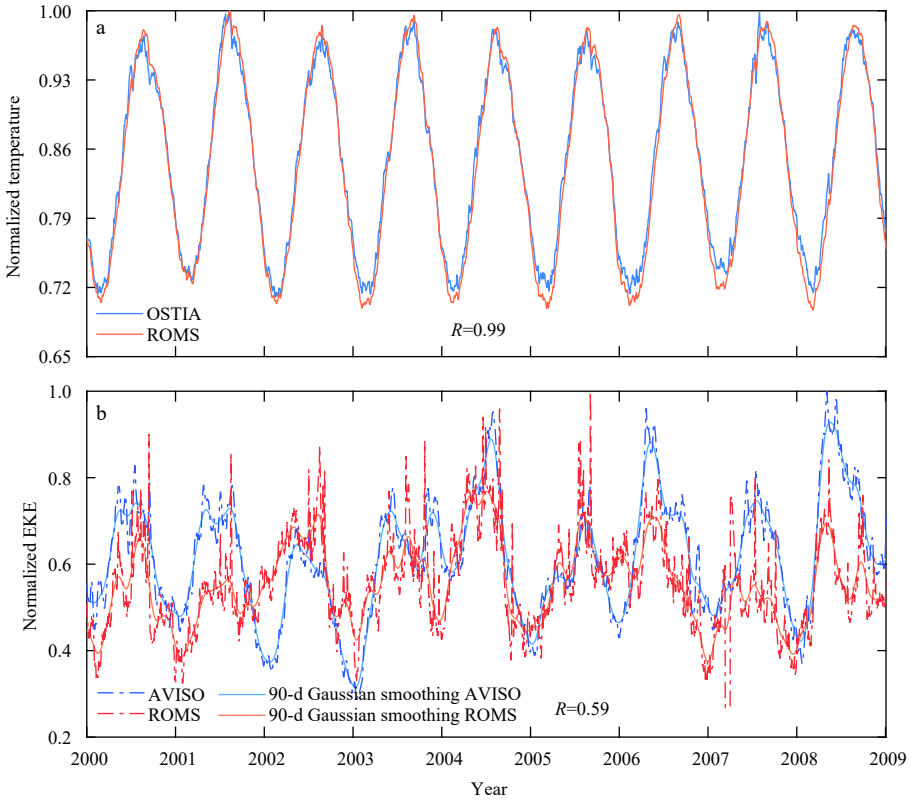

Fig. A2. Time series of normalized SST (a) and EKE (b) in the study area from 2000 to 2008. Normalization means dividing the SST and EKE by their respective maximum values (OSTIA 29.6°C , ROMS 29.0°C ; AVISO 362.1 cm^2/s^2, ROMS 450.6 cm^2/s^2). *R* is the correlation coefficient.

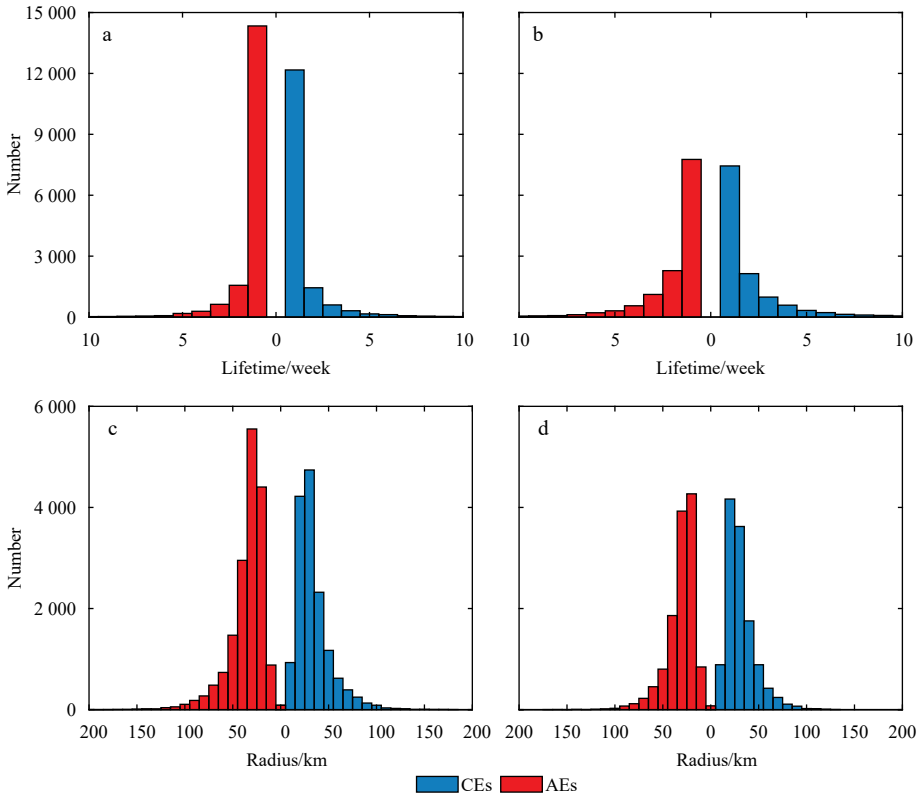

Fig. A3. Histograms of eddy lifetime (a and b) and radius (c and d) from ROMS output (left panels) and the AVISO result (right panels) from 2000 to 2008.

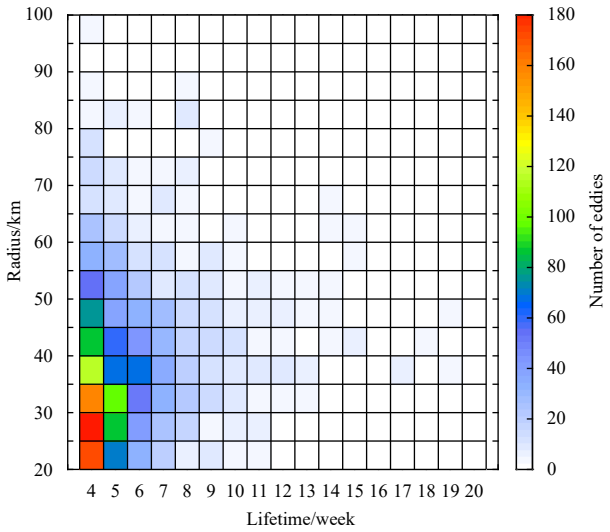

Fig. A4. The eddy number distribution with different lifetimes and radiuses.